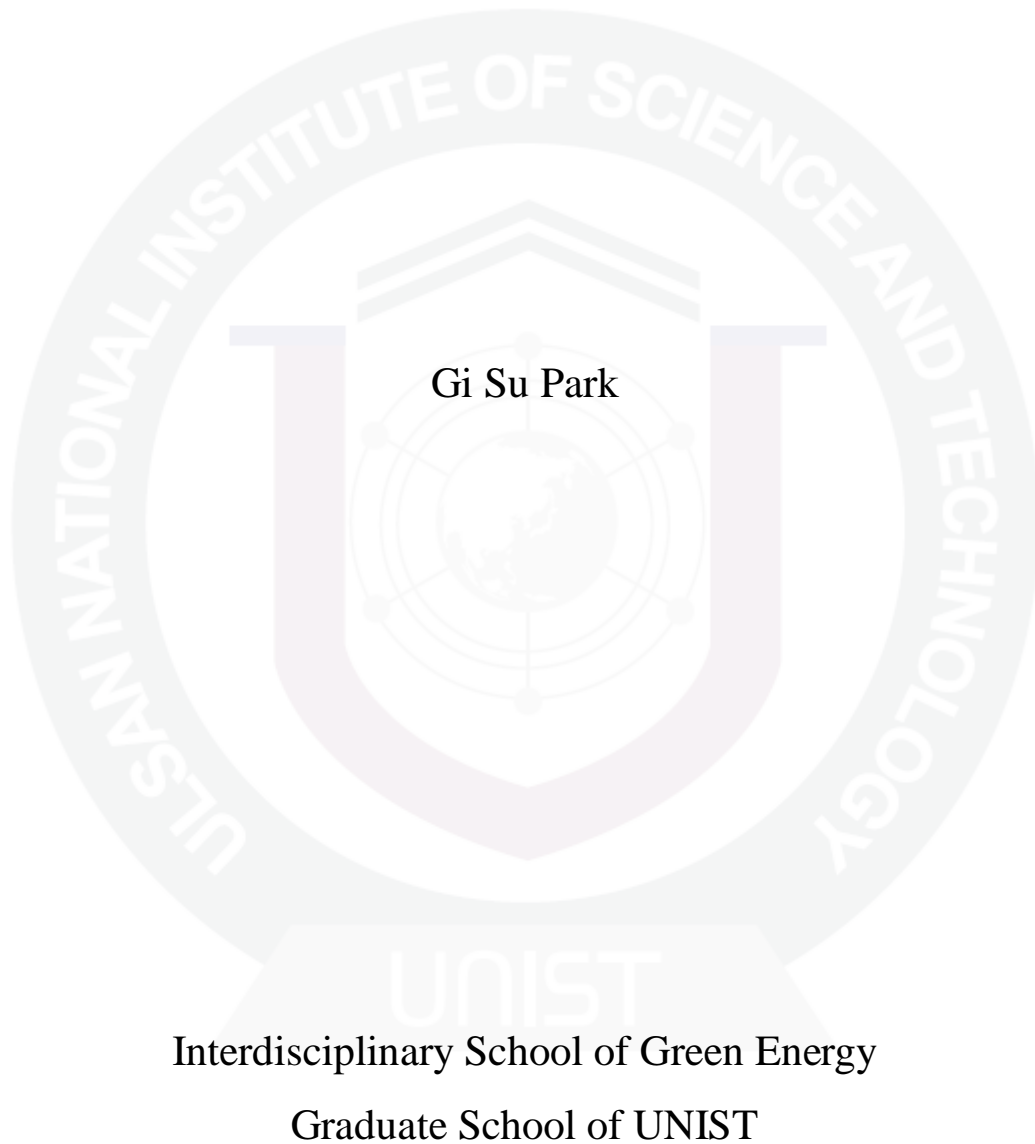


Nitrogen-Doped Carbon Nanofibers as an Highly Efficient Electrocatalyst For Zn-Air Batteries



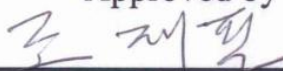
Nitrogen-Doped Carbon Nanofibers as an Highly Efficient Electrocatalyst For Zn-Air Batteries

A thesis
submitted to the Interdisciplinary School of Green Energy
and the Graduate School of UNIST
in partial fulfillment of the
requirements for the degree of
Master of Science

Gi Su Park

2. 8. 2013

Approved by



Major Advisor

[Jaephil Cho]

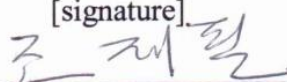
Nitrogen-Doped Carbon Nanofibers as an Highly Efficient Electrocatalyst For Zn-Air Batteries

Gi Su Park

This certifies that the thesis of Gi Su Park is approved.


2. 8. 2013

[signature]




Thesis supervisor: [Jaephil Cho]

[signature]



[Soojin Park]

[signature]



[Byeong-Su Kim]

Contents

Abstract.....	5
Figures and table.....	6
I. INTRODUCTION.....	9
II. REVIEW OF RELATIVE LITERATURE.....	10
2.1 Zinc-air batteries.....	10
2.1.1 Cathode : Air Electrode and Catalysts.....	12
2.1.1.1 Nitrogen-Doped Carbon.....	14
2.2 Electrospinning.....	15
2.2.1 Carbon Nano fibers.....	18
2.2.1.1 Structure and Properties.....	18
III. EXPERIMENT.....	22
IV. RESULTS AND DISCUSSIONS.....	24
V. CONCLUSION.....	37
VI. ACKNOWLEDGEMENTS.....	38
VII. REFERENCES.....	39

Abstract

Nitrogen-doped carbon nanofibers have potential to be an alternative metal-free catalyst for the air-electrodes in fuel cells and metal-air batteries because of their enhanced electro-catalytic activity toward oxygen reduction reaction (ORR). However, the available nitrogen doping processes require more than one step. Here we report a simple and cost-effective fabrication process, electrospinning of polymeric fibers followed by carbonization at 1100°C, for preparation of nitrogen-doped porous carbon nanofibers with extremely high surface area (1271 m²g⁻¹), demonstrating excellent electrocatalytic activity toward ORR at low cost, which is attributed to proper nitrogen-doping and enhanced graphitic characteristics of carbon fibers. For example, the performance of a Zn-air cell based on the nitrogen-doped porous carbon nanofibers exhibits a peak power density of 194 mW/cm², comparable to that based on a commercial Pt/C catalyst (192 mW/cm²). Further, the generation of hydrogen peroxide ion (< 20%) in a half cell on the new catalyst is similar to that on the commercial Pt/C catalyst.

Figure captions

Figure 1. Working principle and each electrode reaction of zinc-air battery. Note the red circle where three phase reaction (oxygen (gas), catalysts (solid) and electrolyte (liquid)) occur in air cathode.

Figure 2. Schematic polarization curves of zinc-air cell. The equilibrium potential of the zinc-air cell (black line) is 1.65 V, but the practical voltage (red line) in discharge is lower than 1.65 V due to the sluggish ORR. A large potential is needed to charge zinc-air battery, higher than the equilibrium potential (blue line).

Figure 3. Trends in oxygen reduction activity (defined in the text) plotted as a function of the oxygen binding energy. Reprinted with permission. Copyright 2004, American Chemical Society.

Figure 4. Nitrogen species commonly reported in post pyrolyzed nitrogencontaining carbon.

Figure 5. Comparison of the XPS spectra of the N 1s region for Vulcan carbon treated 2 h at 900 °C with acetonitrile: (a) sample exposed to atmosphere; (b) sample transferred to XPS via a controlled atmosphere transfer chamber.

Figure 6. XPS spectra of the C 1s regions demonstrating the widening of the C 1s peak in a sample containing nitrogen.

Figure 7. Schematic illustration of the basic setup for electrospinning. The insets show a drawing of the electrified Taylor cone and a typical SEM image of the nonwoven mat of poly(vinyl pyrrolidone) (PVP) nanofibers deposited on the collector.

Figure 8. Photographs illustrating the instability region of a liquid jet electrospun from an aqueous solution of poly(ethylene oxide) (PEO). The capture time was on two different scales: A) 1/250 s, and B) 18 ns, respectively. Note that the path of the jet shown in B has been traced to improve the visibility. Copyright Elsevier Science, 2001.

Figure 9. TEM images showing the representative microstructures of (A) low temperature (1000 °C) carbonized PAN nanofibers, and (B) high temperature (2200 °C) carbonized PAN nanofibers.

Figure 10. a–c) Cross-sectional images of thermally treated nanofibers at 2800 °C PAN:PMMA= a) 5:5, b) 7:3, and c) 9:1. d) TEM image of sample (a) showing structurally developed core walls after thermal treatment.

Figure 11. Polyacrylonitrile (PAN) and polystyrene (PS) were dissolved in dimethylformamide (DMF) as a carbon precursor. Nitrogen-doped porous carbon nanofibers were obtained after electrospinning and pyrolysis at 1100 °C to investigate the electrocatalytic activity for ORR.

Figure 12. A typical SEM image of (a) NPCNFs-800, (b) NPCNFs-900, (c) NPCNFs-1000, (d) NPCNFs-1100. The interconnected carbon nanofiber webs of NPCNFs-1100 offer a continuous electron pathway to enhance efficient current collection.

Figure 13. TEM images of a NPCNFs-1100 sample prepared from carbonization at 1100 °C for 1h in nitrogen showing the porous structure.

Figure 14. XRD patterns of NPCNFs carbonized at different temperatures (800°C to 1100°C). The patterns show that samples are composed of disordered carbon (hard carbon).

Figure 15. Nitrogen adsorption-desorption isotherm of (a) NPCNFs-800, (b) NPCNFs-900, (c) NPCNFs-1000, and (d) NPCNFs-1100 samples.

Figure 16. Pore size distribution of (a) NPCNFs-800, (b) NPCNFs-900, (c) NPCNFs-1000, and (d) NPCNFs-1100 samples.

Figure 17. Cyclic voltammograms of NPCNFs-1100 and CNF-1000 samples obtained at a scan rate of 100mV/s in argon saturated 0.1 M KOH solution (stirring at 1600 rpm). The electrochemically active surface area (ECSA) of NPCNFs-1100 is approximately 2.5 times higher than CNF-1000.

Figure 18. SEM images of a unmodified PAN based carbon fiber carbonized 1000 °C in N₂ atmosphere (CNF-1000). b Nitrogen-doped porous carbon nanofiber obtained via carbonized at 1100 °C in N₂. The image shows formation of inner and outer pores consisting of meso- and micro-structures. The deconvoluted high-resolution N1s XPS spectra of c NPCNFs-800, d NPCNFs-900, e NPCNFs-1000, and f NPCNFs-1100. These peaks were fitted mainly into four components centered at around 398.0, 400.0, 401.3, and 402-405 eV, corresponding to pyridinic N (Dark Cyan), pyrrolic N (Orange), graphitic N (Navy), and pyridinic N oxide (Olive), respectively.

Figure 19. Converted values of N-species of each samples in Table S2.

Figure 20. Some typical XPS spectra of C1s for NPCNFs.

Figure 21. Raman spectra of NPCNFs after thermal treatment at different temperatures. The number adjacent to each spectrum represents the I_D/I_G ratio, which diminished with increasing pyrolysis temperature. Also, the G band became shaper with higher peak intensity at higher pyrolysis temperature.

Figure 22. (a) Polarization curves of a NPCNFs-1100 sample in O_2 -saturated 0.1M KOH electrolyte collected at different rotation rates at a scan rate of 10 mV/s, (b) Koutecky-Levich plots of the NPCNFs-1100 sample at potential -0.4, -0.5, -0.6, and -0.7 V vs. Hg/HgO.

Figure 23. (a) Ring and disk current density in O_2 -saturated 0.1M KOH at a rotation rate of 2500 rpm. The disk potential was scanned at 10mV/s and the ring potential was kept constant at 0.3V (vs. Hg/HgO). (b) and (d) The number of electrons transferred and the percentage of peroxide at different potential range, respectively. (c) The kinetic-limiting current density at -0.15 V (vs. Hg/HgO).

Figure 24. Electrochemical half-cell data of Pt/C catalysts. (a) Ring and disk current density in O_2 -saturated 0.1M KOH at a rotation rate of 2500 rpm. The disk potential was scanned at 10mV/s and the ring potential was kept constant at 0.3V (vs. Hg/HgO). (b) and (d) The number of electrons transferred and the percentage of peroxide at different potential range, respectively. (c) The kinetic-limiting current density at -0.15 V (vs. Hg/HgO).

Figure 25. Cyclic voltammograms (the 1st and the 300th) of NPCNFs-1100 and 20 wt% Pt/C samples at a scan rate of 50 mV/s in argon saturated 0.1M KOH solution to show the stability during cycling.

Figure 26. (a) a zinc-air cell consisted of an air cathode, a separator, and a zinc powder anode with 6M KOH. (b) the air electrode divided into gas diffusion layer (GDL), catalyst layer(NPCNFs-1100), and Ni mesh as a current collector. (c) polarization curve with a scan rate of 5 mA/cm²-sec and d corresponding power density curves at a constant current density varied from 0 to 340 mA/cm².

Table captions

Table 1. Physicochemical characterization of CNF-1000, NPCNFs-800, NPCNFs-900, NPCNFs-1000, and NPCNFs-1100.

Table 2. Characteristics of the PAN-based porous carbon nanofibers reported in previous studies.

Table 3. Detailed breakdown of N 1s spectra from the NPCNFs samples from XPS analysis, indicating relative atomic ratios of N species.

I. INTRODUCTION

Metal-air batteries and fuel cells have attracted much attention due to their low cost, relatively high capacity, easy handling, and environmental benignity.[1-3] However, the performance of these electrochemical devices is primarily limited by the sluggish oxygen reduction reaction (ORR) kinetics. Accordingly, Pt-based catalysts have been widely used to enhance the ORR;[4-6] however, they are very expensive and have limited availability. Nitrogen atoms doped in a carbon plane with lone pair of electrons are reported to significantly enhance the electrocatalytic activity for oxygen reduction reaction (ORR).[7-14] Although many different approaches have been studied for doping nitrogen into graphene, including nitrogen plasma treatment[15], chemical vapor deposition of methane in NH_3 [16] and electrothermal reaction in NH_3 ,[17] they require multiple steps to functionalize nitrogen atoms on carbon-based materials such as carbon nanotube[18] and graphene.[19] In contrast, nitrogen-doped carbon nano-fibers can be easily fabricated using nitrogen-containing compounds through electrospinning, which is a simple, convenient, and versatile technique widely used for fabrication of extremely long nanofibers with diameters ranging from tens of nanometers to a few micrometers.[20-25]

Here we report a highly-active electrocatalyst based on nitrogen-doped carbon nanofibers for ORR, which is as efficient as a commercial Pt/C catalyst but at much lower cost. The dramatically enhanced electrocatalytic activity of the electrospun carbonfibers is attributed to their unique molecular structure under proper processing conditions: more nitrogen atoms were doped at the edge of carbon planes and a churros-like porous structure with very high surface area was created at high carbonization temperatures. Further, when used as the cathode in a Zn-air cell, power density of $\sim 194 \text{ mWcm}^{-2}$ was demonstrated, which is comparable to that of a similar cell based on a commercial Pt/C catalyst ($\sim 192 \text{ mWcm}^{-2}$).

II. REVIEW OF RELATIVE LITERATURE

2.1 Introduction to Zinc-air batteries

Zinc-air cells are composed of three parts; zinc metal as an anode, an air electrode as the cathode, which is divided into a gas diffusion layer and a catalytic active layer, and a separator, as shown in **Figure 1**. Because the solubility of oxygen is very low at atmospheric pressure, it is necessary to use oxygen in the gas phase, not liquid.[26, 27] Oxygen from the atmosphere diffuses into the porous carbon electrode by difference in pressure of oxygen between the outside and inside of the cell, and then the catalyst facilitates the reduction of oxygen to hydroxyl ions in the alkaline electrolyte with electrons generated from the oxidation of zinc metal as the anode reaction. This is why we call this process a three-phase reaction: catalyst (solid), electrolyte (liquid), and oxygen (gas). Note in **Figure 1** the red circle where this three phase reaction occurs. This structure favors the gain of oxygen in zinc-air batteries. Generated hydroxyl ions migrate from the air cathode to the zinc anode to complete the cell reaction; this overall procedure during discharge can be described as the following electrochemical reactions of anode and cathode in alkaline solution, respectively.

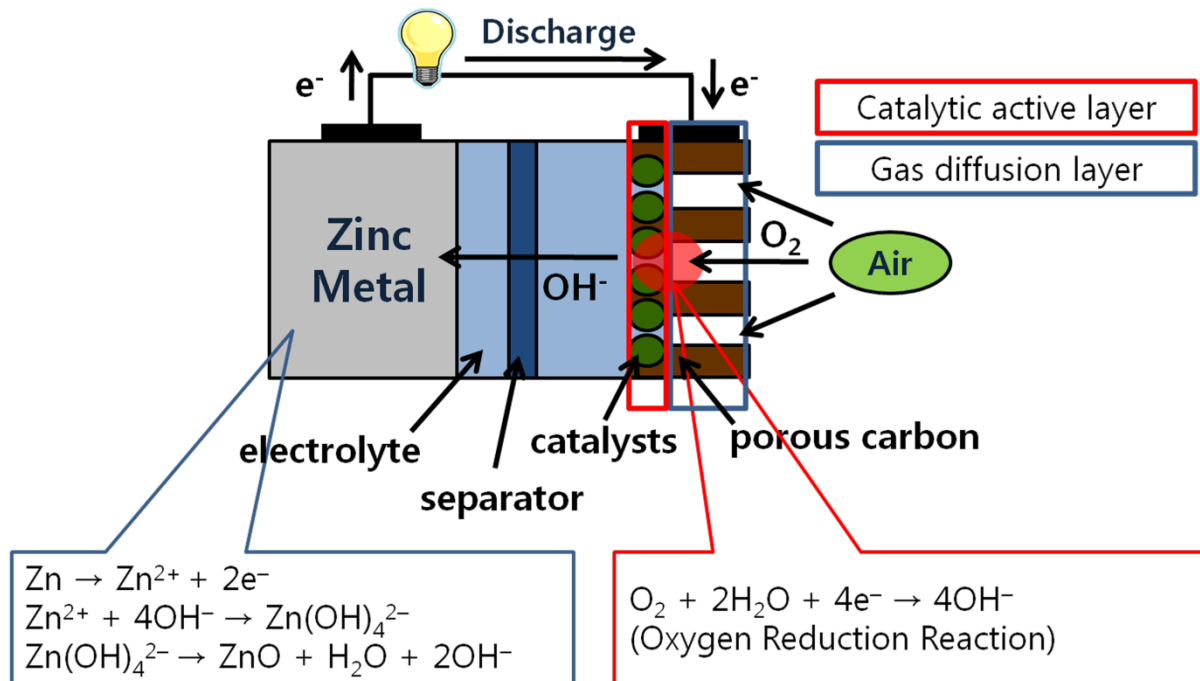
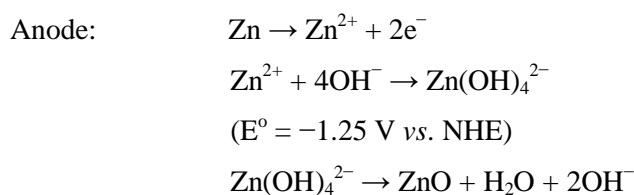
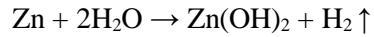
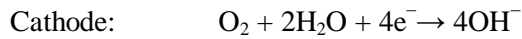


Figure 1. Working principle and each electrode reaction of zinc-air battery. Note the red circle where three phase reaction (oxygen (gas), catalysts (solid) and electrolyte (liquid)) occur in air cathode.[2]

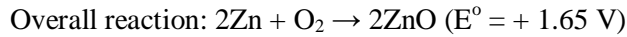




(also possible)



($E^\circ = 0.4 \text{ V vs. NHE}$)



From the above chemical equation, with the exception of HER (which will be discussed later), the equilibrium potential of the zinc-air cell should be 1.65 V, where $E_{\text{eq}} = E_0(\text{cathode}) - E_0(\text{anode})$. However, the practical working voltage of the zinc air cell is less than 1.65 V due to the internal loss of the cell due to activation, and ohmic and concentration loss.[28] In this review, we will not discuss these kinds of electrochemical losses in detail. However, it may be helpful to understand the electrochemical behavior of zinc-air batteries through a schematic polarization curve of each anode and cathode reaction.

Figure 2 is a schematic potential (v)-current (i) curve to efficiently understand the major origin of potential loss in zinc-air cells using oxygen. Note that the overpotential at the zinc anode is relatively smaller than that at the air electrode; also, the cathodic current occurs at the cathode, the air electrode. Conversely the anodic current occurs at the anode, the zinc electrode, in the discharge (red line). Of course, each current direction is reversed upon charging (blue line). From the polarization curve, it is possible to see that a large overpotential (the green line in **Figure 2**) is needed to generate hydroxyl ions by oxygen reduction reaction (ORR). This is why the working voltage of the actual zinc-air cell (E_1 , **Figure 2**, red line) is much smaller than 1.65 V, the open-circuit potential (OCV) (E_{eq} , black line). Considering the reverse reaction (the oxygen evolution reaction) (OER), a larger potential is needed for charging (**Figure 2**, blue line). From the brief discussion above, it can be seen that using the ORR has both positive and negative effects on zinc-air cells. The positive point enables this cell to have large energy density because of the lack of oxygen active material in the cell. We have already discussed this point. The negative point, conversely, forces the zinc-air cell to have significant potential loss, which eventually causes a decrease in the power density of the cell. This is why many studies have focused on how to minimize the large overpotential in the cathode reaction by developing new catalysts and modifying air electrode structures. Of course, when it comes to a primary zinc-air cell, it is not necessary to consider any problem in the zinc anode because the utilized zinc metal can be replaced with fresh metal via mechanical charging. However, for the purpose of developing an electrically rechargeable zinc-air battery, it is also important to study how to improve the electrochemical behavior of the zinc anode. Setting aside these two major drawbacks in zinc-air cells, other problems could still be obstacles in developing a secondary zinc air battery. In this review, we will deal with selected efforts to overcome possible problems in zinc-air cells and also discuss how to approach the development of a secondary zinc-air battery.

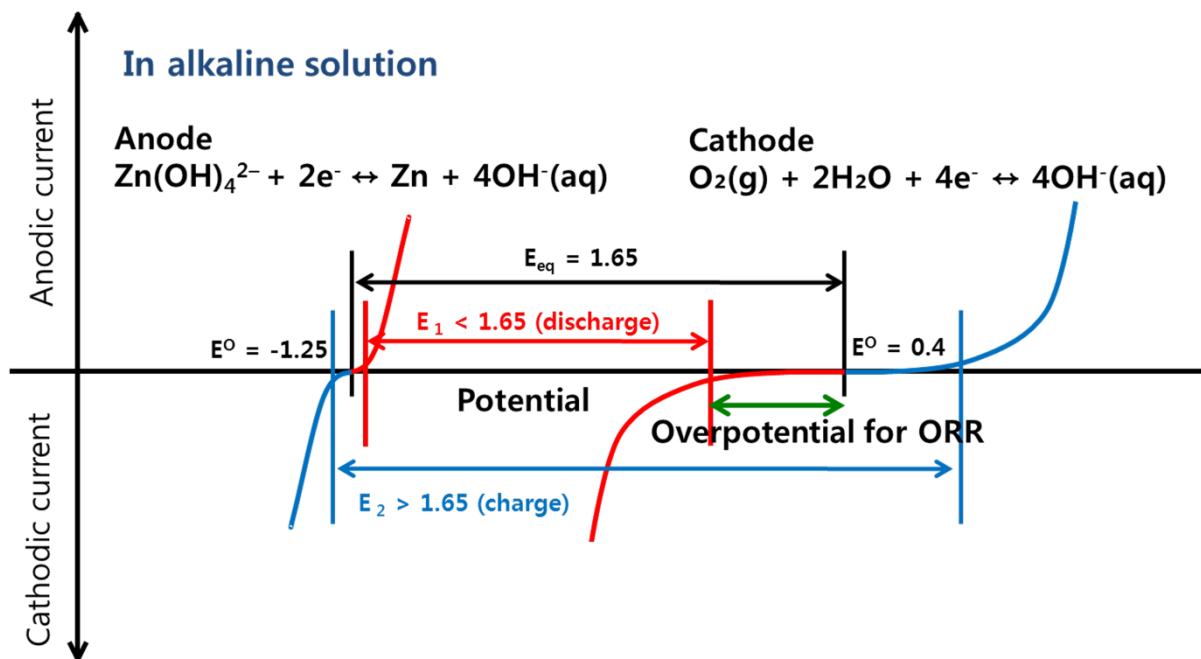


Figure 2. Schematic polarization curves of zinc-air cell. The equilibrium potential of the zinc-air cell (black line) is 1.65 V, but the practical voltage (red line) in discharge is lower than 1.65 V due to the sluggish ORR. A large potential is needed to charge zinc-air battery, higher than the equilibrium potential (blue line).[2]

2.1.1 Cathode : Air Electrode and Catalysts

The concept of using oxygen in a zinc-air battery requires the air electrode to have both proper catalysts for oxygen reduction reaction (ORR) and a highly porous structure. These two requirements should be considered simultaneously for designing an air electrode. As mentioned in the introduction, catalysts are needed to alleviate the large activation energy for ORR, but the structure of the air electrode is also an important factor affecting the performance of the zinc-air cell. In actual fact, the air electrode acts simply as a substrate where ORR occurs. Considering the overall reaction of the zinc-air battery ($2\text{Zn} + \text{O}_2 \rightarrow 2\text{ZnO}$), the only consumed materials are zinc metal and oxygen. Since oxygen is supplied endlessly from the atmosphere, in principle, the air electrode itself can be used repeatedly unless there is physical damage such as cracking in the air cathode after discharge.

The highly porous structure of air electrodes makes a diffusion path for oxygen and functions as a substrate for catalysts. Therefore, carbon materials such as activated carbon and carbon nanotubes (CNT) can be used as substrates for the air electrode. Typically, an air electrode consists of a gas diffusion layer and a catalytic active layer and is prepared by laminating these together with a metal grid as a current collector.[29] (see **Figure 1**) The gas diffusion layer is composed of carbon material and a hydrophobic binder such as polytetrafluoroethylene (PTFE) as a wet-proofing agent. It is important to maintain hydrophobicity, which makes gas diffusion layer permeable to air but not water. The catalytic active layer consists of catalysts, carbon materials, and the binder. It is in the catalytic active layer that the oxygen reduction reaction (ORR) takes place. From the above discussion, it is

reasonable to assume that types and amounts of each material[30] and structure of air electrode[31-34] affect the performance of the air electrode. Eom et al. reported that micropores (0.2 ~ 2 nm) of activated carbon did not affect the performance of the cathode in zinc air batteries.[35] By placing carbon particles in a sinter-locked network of metal fibers, Zhu et al. developed a thin layer air electrode (< 0.15 nm) that is 30 ~ 75% thinner than the commercial air electrode; they suggested that this structure makes the three-phase reaction sites more efficient. [26] To make a secondary zinc-air battery, developing a bifunctional catalyst is important. In addition to the catalyst itself, the oxidation of the catalyst[36] and the carbon substrate should also be considered in air electrodes where the oxygen evolution reaction (OER) takes place during charging, because the high surface area of the carbon substrate is severely attacked by the highly reactive oxygen generated from the OER.[37] Ross and Sattler demonstrated that graphitized carbon led to a reduction of the corrosion rate under anodic conditions in alkaline solutions.[38]

Although the oxygen reduction mechanism is very complex, it is believed that there are two kinds of mechanism. One is a direct four-electron pathway, in which oxygen directly reduces to OH^- ; the other is a peroxide two-electron pathway, in which oxygen indirectly reduces to OH^- via HO_2^- . [39] Because the two-electron process is more common in alkaline solutions, proper catalysts are needed to facilitate the decomposition of HO_2^- into OH^- . It is well known that the kinetics of the oxygen reduction reaction (ORR) are very sluggish and that overpotential is required for the desired reaction. This phenomenon conversely decreases power density and high rate discharge. On the other hand, this problem is a commonly observed one in batteries using oxygen as active material, such as other metal air cells and fuel cells. Therefore, many efforts to overcome this problem have focused on finding proper catalysts to reduce the oxygen reduction overpotential (see **Figure 2**).

Advances in computational catalysis have enabled us to screen inactive catalysts and to predict which catalysts will have more activity for ORR, which prediction helps save time and costs in developing proper catalysts. D-band center theory, suggested by Norskov, has played an important role in studies of catalysts,[40, 41] and a famous volcano plot has been used to predict activity and selectivity of catalysts for ORR when designing better fuel cells[42] as shown in **Figure 3**. Based on this plot, many noble metal catalysts, both alloy and faced-metal catalysts, have been studied to improve ORR activity.[5, 43-49] Although noble metal catalysts such as platinum have high activity for ORR, the cost of manufacturing an air cathode increases dramatically when using such metals, which impedes commercialization. And, because oxygen reduction in alkaline solution is used as the cathode reaction in the zinc-air system, it is not necessary to use a pure noble metal catalyst.[37] With an advantage in the alkaline system, it is possible to use typical transition metal oxides such as perovskite, pyrochlore and spinel, individual oxides, and their mixtures for air cathodes.[37, 39, 50-52] Gorlin et al. reported that Mn oxide thin film showed higher activity for both ORR and OER, similar to that of noble metal catalysts: Pt, Ru, and Ir.[53] Han et al. reported on the dependence of particle

size on the oxygen reduction reaction (ORR). Using cyclic voltammetry and a rotating disk electrode (RDE), they found that the direct four electron pathways were preferred by larger Ag particles (174 nm), and that simultaneous four electron and peroxide two-electron pathways were preferred by finer Ag particles (4.1 nm).[54] Recently, graphene has been used as an ORR catalyst without metal. Qu et al. showed that nitrogen-doped graphene (N-graphene) has much better activity than platinum for ORR via the four electron pathway in alkaline solution; it also has long-term operation stability.[16]

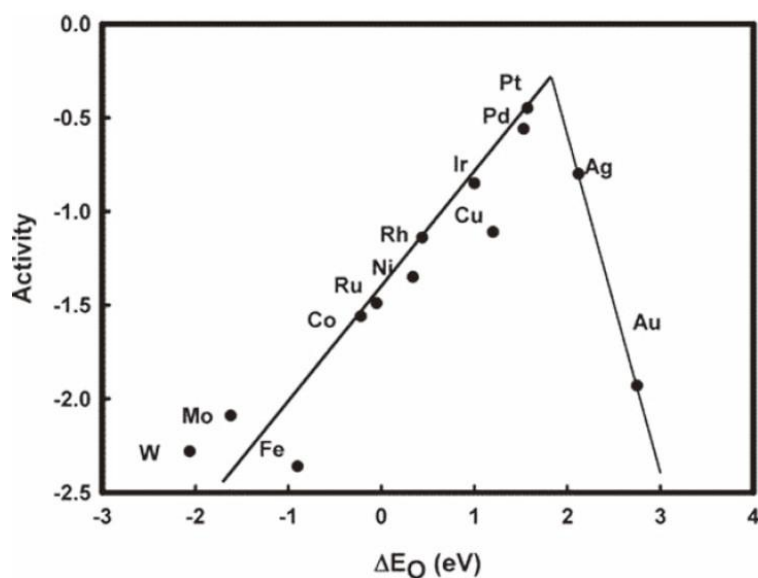


Figure 3. Trends in oxygen reduction activity (defined in the text) plotted as a function of the oxygen binding energy. Reprinted with permission. Copyright 2004, American Chemical Society.[2]

2.1.1.1 Nitrogen-Doped Carbon

Nitrogen-containing carbons have been studied extensively, particularly with XPS, for coal and Li ion battery electrode applications. Pels et al. performed a detailed XPS analysis of the transformation of carbon and nitrogen model compounds into nitrogen-containing graphite during high-temperature pyrolysis [55] and reported that nitrogen functional groups in carbon decompose at higher temperatures to form two species, quarternary nitrogen and pyridinic nitrogen. Quarternary nitrogen can be described as “graphitic nitrogen,” in which nitrogen is within a graphite plane and bonded to three carbon atoms. This type of nitrogen is known to have a characteristic N 1s peak in the XPS spectra at around 401.3 ± 0.3 eV. Pyridinic nitrogen exists on the edge of graphite planes, where it is bonded to two carbon atoms, donates one p electron to the aromatic π -system, and has a resulting N 1s binding energy near 398.6 ± 0.3 eV. Therefore, XPS can be used to quantify these species based on differences in the N 1s spectra.

Although the two previously mentioned nitrogen species are the most stable in carbon treated at high temperatures (>600 °C), some additional nitrogen functional groups are possible in carbon. Pyrrolic nitrogen is often assigned to peaks at 400.5 ± 0.3 eV. Pyridone (pyridinic-N next to an OH group) has

a similar assignment, and the two are considered indistinguishable.[55] Both of these species have been shown to decompose at temperatures above 600 °C to pyridinic-N and quaternary-N.[55] A nitrogen species has also been reported in pyrolyzed samples with a high binding energy (402–405 eV), typical of oxidized nitrogen. Several authors have termed this feature a pyridinic-N⁺-O⁻ species that forms after the sample is exposed to air.[55-57] The species discussed thus far are depicted in **Figure 4**. Computer simulations have shown that the pyridinic-N⁺-O⁻ species can form during the combustion of nitrogen-containing carbon with oxygen.[58]

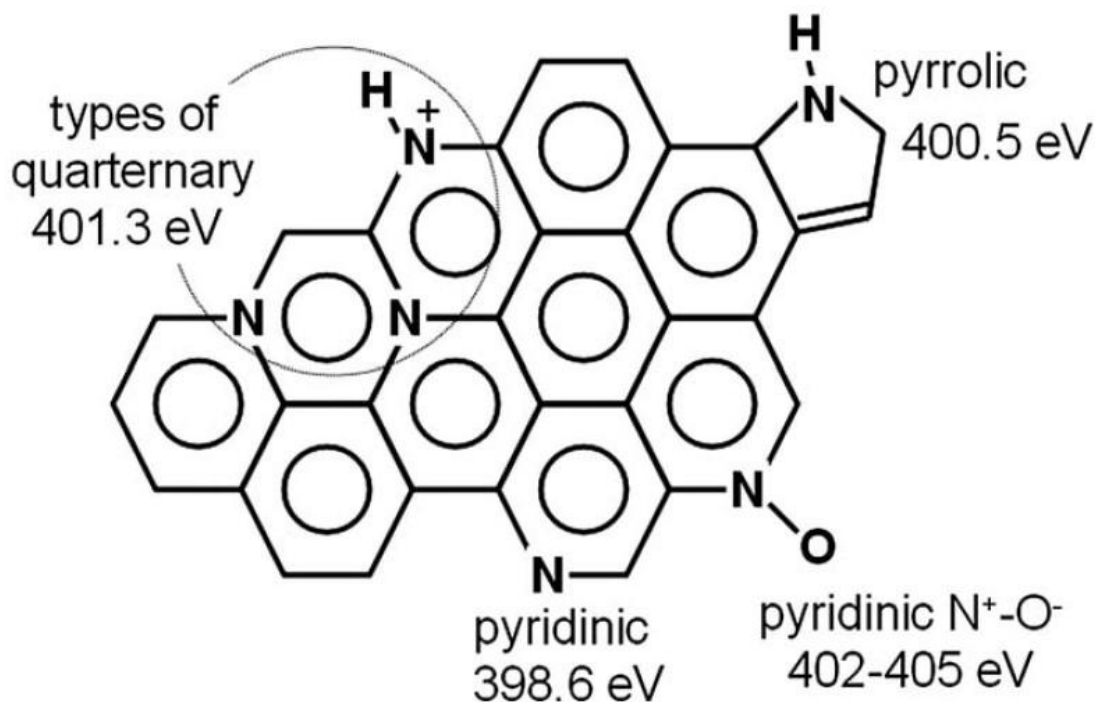


Figure 4. Nitrogen species commonly reported in post pyrolyzed nitrogen-containing carbon.[9]

However, assignment of a pyridinic-N⁺-O⁻ peak cannot be made with a high level of certainty **Figure 5** compares the N 1s region for Vulcan carbon after treatment with acetonitrile at 900 °C for 2 h. The O 1s spectra could not contribute any useful information in this regard because of the low oxygen concentrations on the surface of the samples (<2%) and the wide variety of possible oxygen species on the surface of carbon, thus further reducing the confidence in any deconvolution in this region. Alternative assignments to the high-binding energy shoulder in the N 1s region may be related to the interaction of graphitic nitrogen with other nitrogen atoms or to differences in the binding energy of graphitic nitrogen, depending on its position in the graphite plane. For instance, it has been documented that the presence of nitrogen in graphite stretches the C 1s peak to higher values[59];

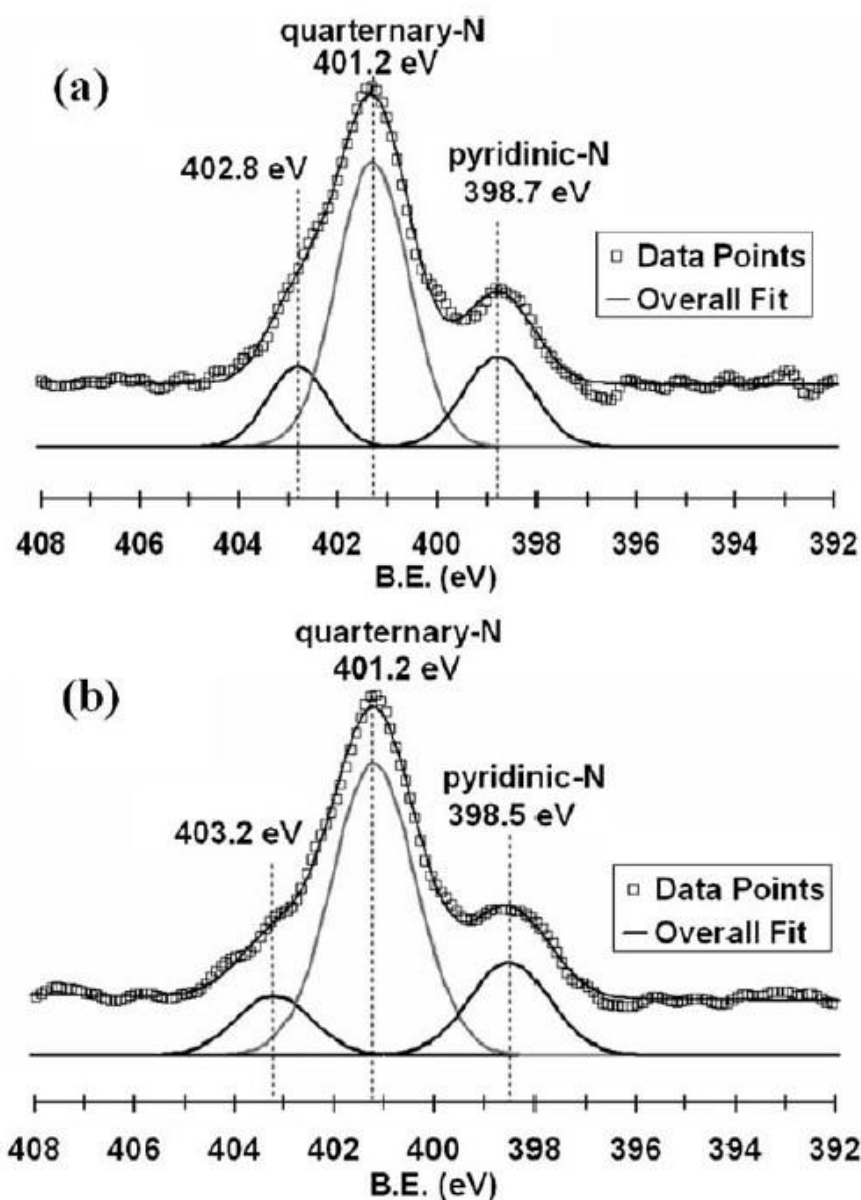


Figure 5. Comparison of the XPS spectra of the N 1s region for Vulcan carbon treated 2 h at 900 °C with acetonitrile: (a) sample exposed to atmosphere; (b) sample transferred to XPS via a controlled atmosphere transfer chamber.[9]

Figure 6 shows an example of this phenomenon. It is possible that because some carbon atoms are closer to a nitrogen atom in the graphite matrix than others, some carbon will inherently have a higher C 1s binding energy. The C 1s peak has been shown to grow wider as more nitrogen is added to graphite.[59] A similar phenomenon may occur in the N 1s spectra. Some nitrogen atoms will be closer to one another and thus have higher binding energy. Alternatively, Casanovas et al. developed a hypothesis to explain this shoulder based on modeling of the binding energy of various nitrogen species present in graphite layers.[60] These authors predicted pyridinic-N and pyrrolic-N to have N 1s binding energies of 399.0 eV and 400.3 eV, respectively, similar to the assignments proposed by Pels et al.[55] However, their calculations revealed that the “graphitic nitrogen” (quarternary-N) can

have a binding energy ranging between 401 and 403 eV, even in the absence of oxidized nitrogen, depending on its location in the carbon plane. Because the cause of the higher-binding energy N 1s shoulder is not obvious, this area of the deconvolution was not assigned. In addition, contributions to the N 1s spectra from pyrrolic nitrogen (or pyridone) were ignored for the samples treated at 900 °C, because such species are not thought to be stable at this temperature,[55] and during deconvolution they appeared to contribute only minimally, if at all. However, samples treated for shorter times and at lower temperatures were difficult to deconvolute in the N 1s spectra, because the nitrogen content was typically lower and perhaps because pyrrolic nitrogen was more abundant. Consequently, only samples treated at 900 °C for 2 h or longer are compared in this work, and for the purposes of this study, the ratio of quaternary to pyridinic nitrogen is of the greatest importance, because this will give some indication to the extent of edge plane exposure and the corresponding nanostructure.

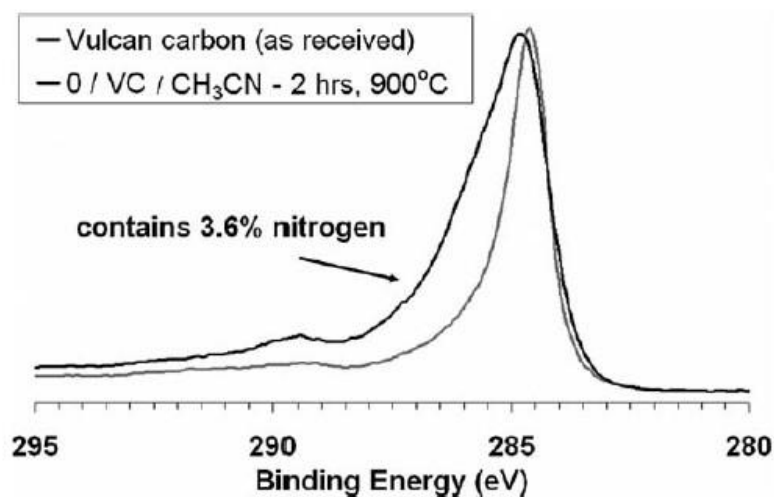


Figure 6. XPS spectra of the C 1s regions demonstrating the widening of the C 1s peak in a sample containing nitrogen. [9]

Lai et al. prepared N-doped RG-O by annealing of G-O under ammonia and found that this material tends to show superior ORR catalytic performance to catalysts produced by annealing of G-O with N containing polymer composites,[7] perhaps due to the considerable content of both pyridinic N and graphitic N. Annealing of PANi/RG-O and Ppy/RG-O gives products containing predominately pyridinic N and pyrrolic N species, respectively. Most importantly, the electrocatalytic activity of N-containing metal-free catalysts is highly dependent on the graphitic N content while pyridinic N species improve the onset potential for ORR. However, the total atomic content of N in the metal-free, graphene-based catalyst did not play an important role in the ORR process. Graphitic N can greatly increase the limiting current density, while pyridinic N species might convert the ORR reaction mechanism from a 2e⁻ dominated process to a 4e⁻ dominated process.[7]

And also it is clearly shown by Geng et al. that nitrogen-doped graphene catalysts can be synthesized by the treatment of graphene by ammonia under different temperatures.[8] The highest ORR activity in alkaline solution was obtained with the catalyst treated at 900 °C. XPS indicated that only 2.8%

nitrogen was introduced into the graphene for N-graphene (900). Quaternary type nitrogen species seem to play the most important role for ORR activity. Moreover, their electrochemical measurements showed that N-graphene (900) catalysts promote the desired $4e^-$ ORR in alkaline solution. In comparison to the commercial Pt/C catalyst, N-graphene (900) catalyst presented higher ORR onset potential (0.308 V) and 43 mV more positive ORR half-wave potential. Also importantly, it demonstrated better stability than Pt/C (loading: $4.85 \mu\text{g}_{\text{Pt}} \text{cm}^{-2}$) in the studied conditions. Therefore, N-doped graphene may have the potential to replace the costly Pt/C catalyst in fuel cells in an alkaline solution.[8]

Matter et al. have concluded that Pyridinic nitrogen itself may not be the active site for the ORR, but may be a marker for edge plane exposure.[9] XPS can possibly give a qualitative measure of edge plane exposure for nitrogen containing carbons, assuming no other nitrogen species present and no additional influence on the formation of quaternary versus pyridinic nitrogen during carbon growth. Based on these insights into the role of nanostructure, there is a large potential for improvement in ORR activity of nonnoble metal materials considering the advancements being made in the formation of carbon nanostructures.[9]

Gong et al. reported that vertically aligned nitrogen-containing carbon nanotubes (VA-NCNTs)[10] can act as a metal-free electrode with a much better electrocatalytic activity, long-term operation stability, and tolerance to crossover effect than platinum for oxygen reduction in alkaline fuel cells. In air-saturated 0.1 molar potassium hydroxide, they observed a steady-state output potential of -80 millivolts and a current density of 4.1 milliamps per square centimeter at -0.22 volts, compared with -85 millivolts and 1.1 milliamps per square centimeter at -0.20 volts for a platinum-carbon electrode. The incorporation of electron-accepting nitrogen atoms in the conjugated nanotube carbon plane appears to impart a relatively high positive charge density on adjacent carbon atoms. This effect, coupled with aligning the NCNTs, provides a four-electron pathway for the ORR on VA-NCNTs with a superb performance.[10]

2.2 Electrospinning

Figure 7 shows a schematic illustration of the basic setup for electrospinning. It consists of three major components: a high-voltage power supply, a spinneret (a metallic needle), and a collector (a grounded conductor). Direct current (DC) power supplies are usually used for electrospinning although the use of alternating current (AC) potentials is also feasible.[61-64] The spinneret is connected to a syringe in which the polymer solution (or melt) is hosted. With the use of a syringe pump, the solution can be fed through the spinneret at a constant and controllable rate. When a high voltage (usually in the range of 1 to 30 kV) is applied, the pendent drop of polymer solution at the nozzle of the spinneret will become highly electrified and the induced charges are evenly distributed over the surface. As a result, the drop will experience two major types of electrostatic forces: the

electrostatic repulsion between the surface charges; and the Coulombic force exerted by the external electric field. Under the action of these electrostatic interactions, the liquid drop will be distorted into a conical object commonly known as the Taylor cone (see the inset of **Figure 7**).[61-63, 65, 66] Once the strength of electric field has surpassed a threshold value, the electrostatic forces can overcome the surface tension of the polymer solution and thus force the ejection of a liquid jet from the nozzle. This electrified jet then undergoes a stretching and whipping process, leading jet is continuously elongated and the solvent is evaporated, its diameter can be greatly reduced from hundreds of micrometers to as small as tens of nanometers. Attracted by the grounded collector placed under the spinneret, the charged fiber is often deposited as a randomly oriented, non-woven mat, see the inset of **Figure 7** for the scanning electron microscope (SEM) image of a typical sample. With the use of this relatively simple and straightforward technique, more than 50 different types of organic polymers have already been processed as fibers with diameters ranging from tens of nanometers to a few micrometers.[61-63]

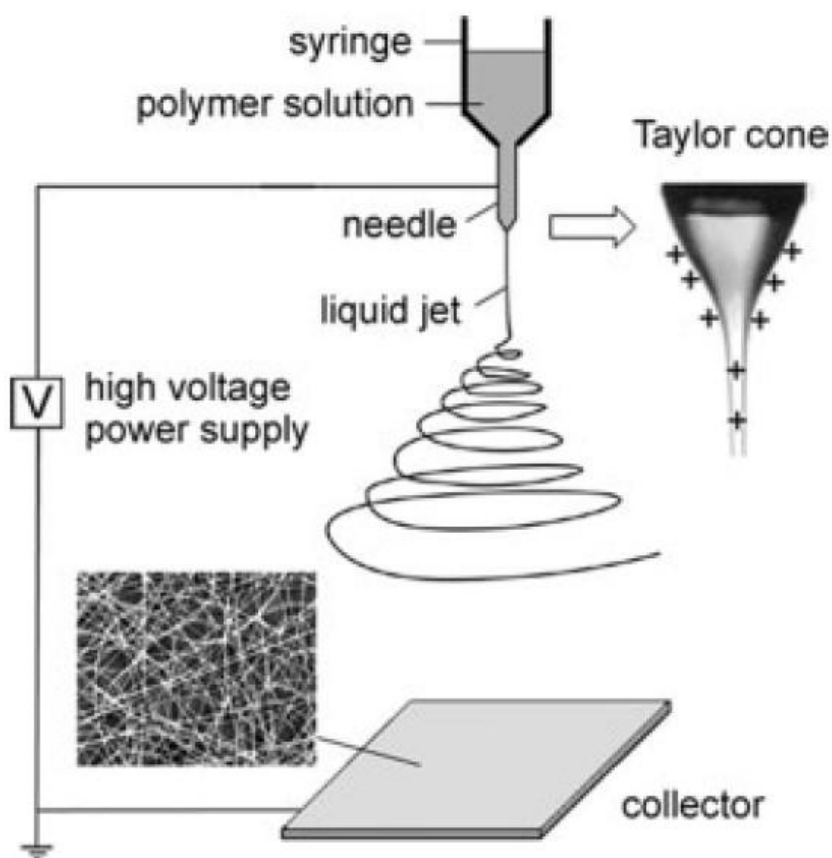


Figure 7. Schematic illustration of the basic setup for electrospinning. The insets show a drawing of the electrified Taylor cone and a typical SEM image of the nonwoven mat of poly(vinyl pyrrolidone) (PVP) nanofibers deposited on the collector.[20]

Although the setup for electrospinning is extremely simple, the spinning mechanism is rather complicated. As in electrospray, electrospinning also involves complex electro-fluid-mechanical issues. Before 1999, the formation of ultrathin fibers by electrospinning was often ascribed to the splitting or splaying of the electrified jet as a result of repulsion between surface charges.[61] Recent

experimental observations demonstrate that the thinning of a jet during electrospinning is mainly caused by the bending instability associated with the electrified jet.[65-68] **Figure 8A** shows the photograph of a spinning jet.[68] It is obvious that the jet was initially a straight line and then became unstable. It appears that the cone-shaped, instability region is composed of multiple jets. However, a closer examination using high-speed photography (**Figure 8B**) establishes that the conical envelope contains only a single, rapidly bending or whipping thread. In some cases, splaying of the electrified jet might also be observed, though it was never a dominant process during spinning.[67, 68] The frequency of whipping is so high that conventional photography cannot properly resolve it, giving the impression that the original liquid jet splits into multiple branches as it moves toward the collector.

Based on experimental observations and electrohydrodynamic theories, mathematical models have been developed by several groups to investigate the electrospinning process. Reneker and co-workers treated the charged liquid jet as a system of connected, viscoelastic dumbbells and provided a good interpretation for the formation of bending instability.[65, 67] They also calculated the three-dimensional trajectory for the jet using a linear Maxwell equation and the computed results were in agreement with the experimental data. Rutledge and co-workers considered the jet as a long, slender object and thereby developed a different model to account for the electrospinning phenomenon.[68-71] Their experimental and theoretical studies clearly showed that the spinning process only involves whipping (rather than splaying) of a liquid jet. The whipping instability is mainly caused by the electrostatic interactions between the external electric field and the surface charges on the jet. The formation of fibers with fine diameters is mainly achieved by the stretching and acceleration of the fluid filament in the instability region. The same group further showed that the model could be extended to predict the saturation of whipping amplitude, as well as the diameter of resultant fibers.[71] In some related studies, Feng proposed another model to describe the motion of a highly charged liquid jet in an electric field, and the role of nonlinear rheology in the stretching of an electrified jet was also examined.[72, 73] All these studies provide a better understanding of the mechanism responsible for electrostatic spinning process. More importantly, they may assist experimentalists enormously in the design of new setups that may provide a better control over the diameter and structure of electrospun nanofibers.

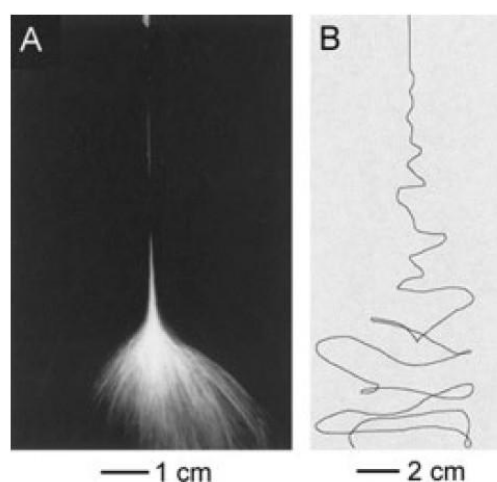


Figure 8. Photographs illustrating the instability region of a liquid jet electrospun from an aqueous solution of poly(ethylene oxide) (PEO). The capture time was on two different scales: A) 1/250 s, and B) 18 ns, respectively. Note that the path of the jet shown in B has been traced to improve the visibility. Copyright Elsevier Science, 2001.[74]

2.2.1 Carbon Nano fibers

In order to convert electrospun polymer nanofibers to carbon nanofibers, carbonization process at around 1000 °C has to be applied. In principle, any polymer with a carbon backbone can potentially be used as a precursor. For the carbon precursors, such as PAN and pitches, so-called stabilization process before carbonization is essential to keep fibrous morphology, of which the fundamental reaction is oxidation to change resultant carbons difficult to be graphitized at high temperatures as 2500 °C. During stabilization and carbonization of polymer nanofibers, they showed significant weight loss and shrinkage, resulting in the decrease of fiber diameter.

Here, the results obtained in these papers are reviewed by dividing into the sections based on the purposes of the research works; fundamental structure and properties of the carbon nanofibers, their performance in energy storage devices, lithium-ion rechargeable batteries and electrochemical capacitors, and composite nanofibers with carbon nanotubes.

2.2.1.1 Structure and Properties

PAN nanofibers were prepared by electrospinning from DMF solution, on which structure and electromagnetic properties were studied.[75-77] Structural analysis was performed on carbon nanofibers, which were prepared from PAN/DMF solution by carbonization at 750 °C followed by 1100 °C.[78] The resultant carbon nanofibers had average diameter of 110 nm, interlayer spacing d_{002} of 0.368 nm and Raman band intensity ratio I_D/I_G of 0.93. From SEM and TEM observations, the fiber was concluded to have skin-core heterogeneity; in the skin carbon layers being oriented predominantly parallel to the fiber surface. PAN-based carbon nanofiber bundles, which were prepared from 10 wt% PAN/DMF solution added 5 wt% acetone and 0.01 wt%

dodecylethyldimethylammonium bromide, and collected on the rim of the rotating disc covered with Al foil, were subjected to the heat treatment at 1400, 1800, and 2200 °C for 1 h.[79] The diameter of nanofibers composing the bundles was approximately 330 nm for as-spun, 250 nm for 1000 °C-treated and 220 nm for 1800 °C-treated. TEM images are shown in **Figure 9** on 1000 °C-treated and 2200 °C-treated nanofibers, the latter having d_{002} of 0.344 nm and I_D/I_G of larger than 1.0. Aiming to have better alignment of basic structural units of hexagonal carbon layers along the fiber axis, multi-walled carbon nanotubes (MWCNTs) were embedded into electrospun PAN-based carbon nanofibers, although the improvement was observed just around MWCNTs.[80] TEM observation on MWCNTs-embedded PAN-based nanofibers by in-situ heating up to 750 °C showed only a local orientation of carbon layers.[81] On PAN-based nanofibers web after the activation by steam at 800 °C, adsorption behavior of benzene vapor was studied at a temperature of 343–423 K under a pressure up to 4.0 kPa, confirming a high adsorption in comparison with activated carbon fiber A-10.[82] By focusing on PAN, electrospinnability, environmentally benign nature and commercial viability were recently reviewed.[83]

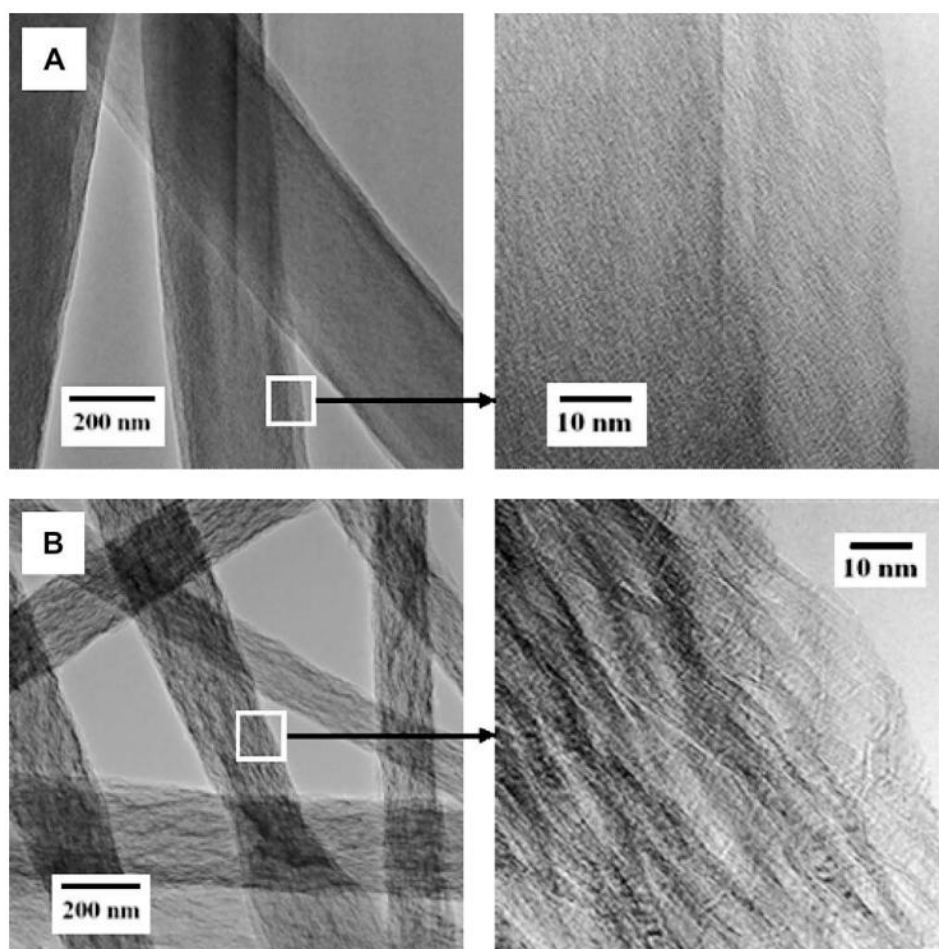


Figure 9. TEM images showing the representative microstructures of (A) low temperature (1000 °C) carbonized PAN nanofibers, and (B) high temperature (2200 °C) carbonized PAN nanofibers.[79]

Core-shell polymeric nanofibers were electrospun through a doubled capillary, PAN/DMF solution

in the outer capillary and poly(methyl methacrylate) PMMA in the inner capillary, and converted to hollow carbon nanofibers by carbonization up to 1100 °C.[84] Similar hollow nanofibers were synthesized by electrospinning of emulsion-like DMF solution of PAN and PMMA in different ratios through a single capillary of 0.5 mm diameter, followed by carbonization at 1000 °C and heat treatment up to 2800 °C,[85] as shown in **Figure 10**. By changing PAN/PMMA ratio, mesopore volume could be controlled; mesopore volume V_{meso} changed from 0.18 cm³ g⁻¹ for 9/1 ratio to 0.47 cm³ g⁻¹ for 5/5 ratio, although micropore volume V_{micro} was almost constant of 0.34 cm³ g⁻¹. [85] Mixing of poly(vinylpyrrolidone) (PVP) into PAN was also employed to control pore structure in the nanofibers.[86] PVP was dissolved out from as-spun fibers at 100 °C under hydrothermal condition and the resultant PAN nanofibers were carbonized at 1000 °C after stabilization. The change of PAN/PVP ratio in the precursor solution from 0.8/0.2 to 0.8/1.0 resulted in the carbon nanofibers with S_{BET} from 237 to 571 m² g⁻¹ and total pore volume V_{total} from 0.10 to 0.19 cm³ g⁻¹. PVP/PAN solutions were separately fed into the spinneret to form side-by-side bicomponent nanofibers and compared with PAN/PVP blend nanofibers after carbonization up to 970 °C and their activation at 850 °C in CO₂. [87] Side-by-side bicomponent nanofibers changed the cross-section morphology from round to cocoon-like shape by PVP extraction.

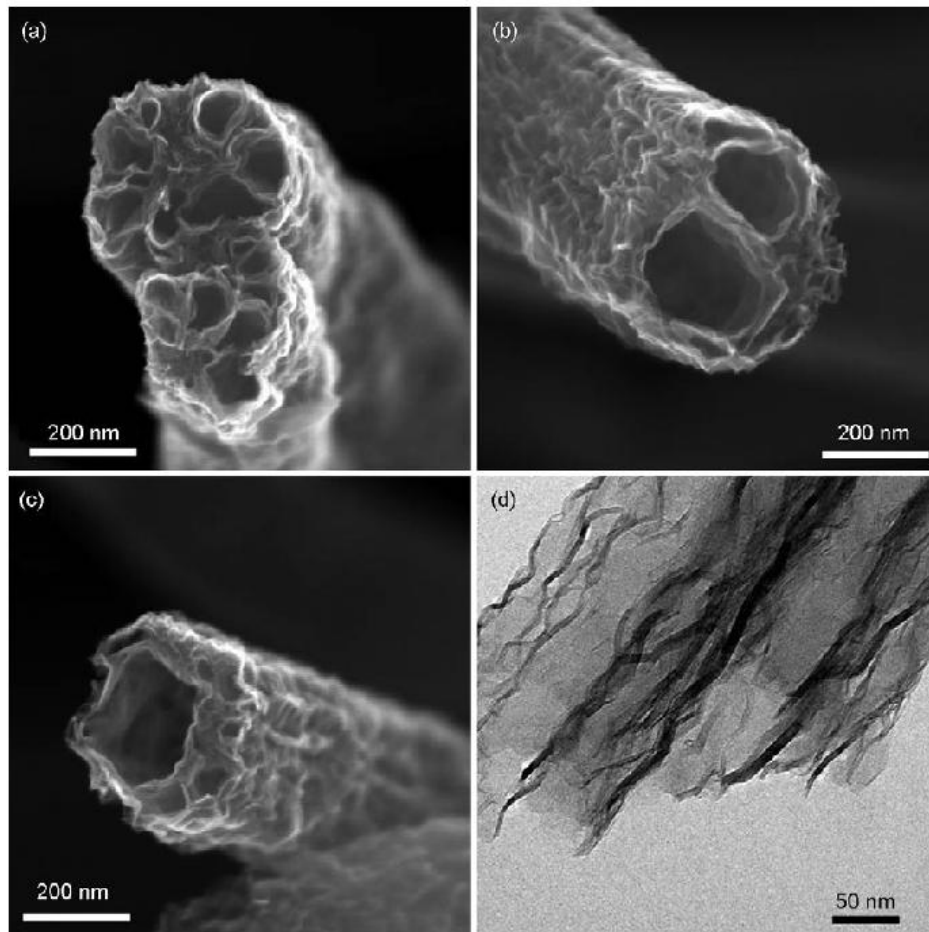


Figure 10. a–c) Cross-sectional images of thermally treated nanofibers at 2800 °C PAN:PMMA= a) 5:5, b) 7:3, and c) 9:1. d) TEM image of sample (a) showing structurally developed core walls after thermal treatment.[85]

The DMF-insoluble fraction of a petroleum-derived isotropic pitch in THF solution (40 wt% pitch) was successfully electrospun to form the web of carbon fibers with 2-6 μm diameter.[88, 89] The difficulty to prepare thinner fiber was pointed out to be resulted from the low boiling point (65–67 $^{\circ}\text{C}$) of the solvent THF, the viscosity of the jet increasing due to the volatilization of THF during electrospinning. After activation, the webs were microporous, showing very high S_{BET} as 2200 $\text{m}^2 \text{g}^{-1}$. By mixing PAN with a pitch, spinnability using a binary solvent DMF + THF (1/1) was improved, resulting in the fibers with the diameter of 750 nm.[90] After activation by using steam at 900 $^{\circ}\text{C}$, S_{BET} of 1877 $\text{m}^2 \text{g}^{-1}$ and V_{total} of 1.11 $\text{cm}^3 \text{g}^{-1}$, consisting of both micro- and meso-pores, were obtained. THF soluble component of the pitch with a low molecular weight of 556 gave better spinnability on its 40 wt% THF solution, but the carbon nanofibers prepared from a high molecular weight pitch as 2380 showed higher development of micropores, giving S_{BET} of 2053 $\text{m}^2 \text{g}^{-1}$, after carbonization at 1000 $^{\circ}\text{C}$ and activated at 900 $^{\circ}\text{C}$ in steam/ N_2 flow. Highly porous carbon nanofibers were obtained by electrospinning of THF solution of polycarbosilane, followed by pyrolysis at different temperatures and chlorination to extract Si.[91] The nanofibers pyrolyzed at 900 $^{\circ}\text{C}$ and chlorinated at 850 $^{\circ}\text{C}$ had very high S_{BET} as 3116 $\text{m}^2 \text{g}^{-1}$ and V_{total} of 1.66 $\text{cm}^3 \text{g}^{-1}$, which were reported to have a high storage capacity for hydrogen as 3.86 wt% at 17 bar and 77 K.

Polyimide (PI) was also spun to prepare carbon nanofibers.[92-96] Carbon nanofibers prepared from a PI of PMDA/ODA with the diameter less than 2-3 μm could give relatively high tensile strength as 74 MPa and electrical conductivity of 5.3 S cm^{-1} after the heat treatment at 2200 $^{\circ}\text{C}$.[92] A thermotropic PI (Matimid 5218) dissolved into dimethylacetamide (DMAc) together with 0.3–3.0 wt% iron(III) acetylacetonate (AAI) was spun to nanofibers in the atmosphere with 24% humidity and then carbonized at 400–1200 $^{\circ}\text{C}$.[94] It was declared that AAI worked as a catalyst after decomposing to $\alpha\text{-Fe}$ and Fe_3O_4 during carbonization, although the structure parameters changed a little, d_{002} decreasing from 0.37 to 0.34 nm, $L_c(002)$ increasing from 1.0 to 4.2 nm. The addition of PAN in PI solution improved spinnability and decreased the diameter of resultant carbon fibers.[96]

Poly(vinylidene fluoride) (PVDF) nanofibers were spun from the solution of DMF with poly(ethylene oxide) (PEO) and water, of which the webs were dehydrofluorized by using 1,8-diazabicyclo[5,4,0]undec-7-ene at 90 $^{\circ}\text{C}$, followed by carbonization at 1000 $^{\circ}\text{C}$ for 1 h in N_2 to convert to carbon nanofiber webs.[97] They contained three kinds of pores; the largest pores were the interstices among nanofibers, intermediate-sized pores with 100-300 nm size were formed on the fiber surface due to liquid-liquid phase separation and the micropores were due to the decomposition of PEO during carbonization. Dehydrofluorination process was found to be the key to retain the pore morphology in as-spun fibers during carbonization.

For electrospinning of phenolic resin (novolac type), its concentration had to be selected, the solution with more than 65 wt% was difficult to be spun and that with less than 50 wt% gave fibers having beads. Spinnability of phenolic resin solution was improved by the addition of a small amount

of poly(vinyl butyral) (PVB) with a molecular weight (Mw) of 110,000, 1 to 3 wt%. The resultant carbon nanofiber fabrics prepared at 900 °C were flexible and had S_{BET} of ca. 500 m²/g. Addition of a high molecular weight PVB (Mw of 340,000) markedly improved the spinnability of phenolic resin solution due to decreasing solution viscosity and the addition of an electrolyte (pyridine or Na₂CO₃) allowed to give thinner fibers because of increasing electrical conductivity of the precursor solution; 0.1 wt% Na₂CO₃ resulting in the carbon nanofibers with an average diameter of 110 nm and S_{BET} of 790 m² g⁻¹. Microporous carbon nanofibers having V_{micro} of 0.9 cm³ g⁻¹ were prepared from novolactype phenol-formaldehyde by adding PVB and Na₂CO₃, followed by carbonization at 800 °C without activation.[98] Electrical conductivity of these carbon nanofiber fabrics was 5.29 S cm⁻¹. Carbon nanofibers with a narrow pore size distribution of 0.4–0.7 nm were prepared from novolactype phenolic resin via electrospinning of its methanol solution, curing in formaldehyde/HCl and carbonization at 800 °C.[98] Even though no activation was applied, the nanofibers had S_{BET} of 812 m² g⁻¹, V_{total} of 0.91 cm³ g⁻¹ and relatively low $I_{\text{D}}/I_{\text{G}}$ of 0.88.

Electrical conductivity was measured to be 4.9 S cm⁻¹ on 800 °C-carbonized PAN-based carbon nanofibers[75] and the 1000 °C-treated nanofibers showed a large negative magnetoresistance, -0.75 at a temperature of 1.9 K under a magnetic field of 9 T.[77] Although the papers have said that fibrous morphology was survived under the heat treatment, it has to take into account that these nanofibers are not stabilized before carbonization when these properties were compared with those of commercial PAN-based carbon fibers. The PAN-based carbon nanofiber bundles prepared by carbonization at 2200 °C showed the conductivity of 840 S cm⁻¹ in parallel with fiber axis, but 61 S cm⁻¹ in perpendicular to the fiber axis.[79] Electrospun PAN-based carbon nanofibers showed electrical conductivity changes sensitive to NO gas after activation through immersion into 80 wt% H₃PO₄ aqueous solution for 12 h and then heat treatment at 750 °C in Ar.

Mechanical property measurements on single fibers were carried out on PAN-based carbon nanofibers.[78] Averaged bending modulus was measured to be 63 GPa by mechanical resonance method and Weibull fracture stress was 640 MPa with a failure probability of 63%. Tensile strength and Young's modulus measured on the bundles of electrospun PAN-based carbon nanofibers were 542 MPa and 58 GPa, respectively.[79] These mechanical properties reported on electrospun carbon nanofibers are much inferior to commercially available PAN-based carbon fibers. Since oxidative stabilization of PAN fibers has been known to be the most important unit-process for PAN-based carbon fibers, optimization of stabilization condition for electrospun PAN nanofibers has to be studied in detail. Relatively high tensile strength and Young's modulus were reported on electrospun single nanofibers prepared from 9 wt% PAN/DMF solution, followed by stabilization at 300 °C for 1 h in air and carbonized at 800, 1100, 1400 and 1700 °C in N₂. [99] Tensile strength depended strongly on heat treatment temperature, showing the maximum of 2.30 GPa at 1400 °C, and Young's modulus increased with increasing temperature, giving 181 GPa at 1700 °C. These changes in mechanical

properties with heat treatment were explained by the growth of crystallite in nanofibers. However, it has to be pointed out that orientation of crystallites in the nanofibers is randomly oriented, not axial. Stretching on as-spun PAN nanofiber bundles was applied before and during their stabilization, expecting well-developed nanotexture and high mechanical properties,[83, 100] although no detailed experimental data were presented regrettably.

Loading of nanoparticles of various metals and metal oxides were performed via electrospinning process. Various transition metal nanoparticles were loaded to carbon nanofibers in order to improve the performance of electrochemical capacitors and lithium-ion rechargeable batteries, and also loading of platinum to carbon nanofiber webs was carried out for fuel cell applications, as described separately in the following sections. By electrospinning of lignin/ethanol solution containing 0.2 and 0.4 wt% Pt acetylacetonate, followed by stabilization at 200 °C in air and carbonization at 600–1000 °C, microporous Pt-loaded carbon nanofibers were obtained.[101] Pd-loaded carbon nanofibers were prepared from 8 wt% PAN/DMF solution containing 4.8 wt% Pd acetate Pd(OAc)₂ by electrospinning, accompanying by the stabilization in steps from 230 to 300 °C and carbonization at 1100 °C.[102] The resultant nanofibers showed high electrocatalytic activity toward the reduction of H₂O₂. Magnetic CoFe₂O₄ nanoparticles were embedded in PAN-based carbon nanofibers via electrospinning of PAN/DMF solution with dispersed oleic acid-modified CoFe₂O₄ nanoparticles with 5 nm size, followed by stabilization and carbonization.[103] CoFe₂O₄-embedded nanofibers were superparamagnetic because of nanosized magnetic particles and saturation magnetization increased from 45 to 63 emu g⁻¹ by carbonization. SiO₂-embedded carbon nanofibers were prepared by electrospinning of PAN/DMF solutions containing different amounts of SiO₂, followed by stabilization and carbonization.[104] SiO₂ particles embedded in carbon nanofibers were washed out by HF, but S_{BET} and V_{total} increased only to 340 m² g⁻¹ and 0.472 cm³ g⁻¹. Vanadium embedded carbon nanofibers were prepared by electrospinning of PAN/DMF solutions containing different amounts of V₂O₅. [105] After activation by using KOH at 750 °C, nanoporous nanofiber were obtained, S_{BET} reaching to 2780 m² g⁻¹, V_{total} to 2.67 cm³ g⁻¹ and V_{micro} to 1.52 cm³ g⁻¹, which gave a hydrogen storage capacity of 2.41 wt% at 303 K and 10 MPa. Mn-loaded carbon nanofibers, which were activated by steam at 850 °C and had V_{micro} of 0.42 cm³ g⁻¹, gave relatively high adsorption capacity for toluene at 289 K.[106]

III. EXPERIMENT

The polymer blend solution for electrospinning was prepared by dissolving polyacrylonitrile (99.9%, PAN, $M_w = 150,000$ g/mol, purchased from Aldrich) and Polystyrene (99.9%, PS, $M_w = 230,000$ g/mol, purchased from Aldrich) in N,N-dimethylformamide (DMF) with the concentration of 10 wt% and 6 wt%, respectively. This blend solution was stirred at room temperature for 24 h to attain homogeneous solution. The PAN/PS fibers were fabricated by a homemade electrospinning setup, which consisted mainly of a high voltage power supply (0-30kV), an ordinary syringe with a plastic nozzle (25G, Nano NC, Korea), and a syringe pump. Aluminum foil was used as the collector. The electrospinning was carried out at a fixed voltage of 15 kV and a tip-to-collector distance of 15 cm. The electrospun nanofibers were oxidized in air at 400 °C for 1h, and then carbonized at 800, 900, 1000, and 1100 °C for 1h in N₂ atmosphere. The obtained samples were denoted as NPCNFs-800, NPCNFs-900, NPCNFs-1000 and NPCNFs-1100, respectively.

Catalyst ink was prepared by ultrasonically mixing 2.0 mg as-prepared sample with 1.0 mL of 0.05% nafion (Aldrich) dispersion solution in DI-water for 1 h in order to make homogeneous suspension. Then, 6 μ L of the prepared catalytic ink was transferred to the surface of a glassy carbon electrode of 5 mm diameter using a micropipette. The ink was then dried for 15 min under vacuum at room temperature to form thin catalyst film on glassy carbon electrode as a working electrode Pt/C sample was obtained from Premetec. (20 wt% Pt on Vulcan XC-72).

All half-cell experiments for ORR activity study using rotating disk electrode (RDE) and rotating ring disk electrode (RRDE) (ALS Co., Ltd) were carried out in 0.10 M KOH electrolyte under the same conditions using Pt wire and Hg/HgO as the counter and the reference electrode, respectively; Oxygen gas (99.9%) was purged for 30 min before each RDE and RRDE experiments to ensure that the electrolyte was saturated with oxygen. Rotation speed was varied from 900 to 2500 rpm to determine the kinetic parameters relevant to ORR using Koutecky-Levich equation. Electrochemical characterization of as-prepared catalysts was performed using a potentiostat (Ivium) at a scan rate of 10 mV/sec in the potential range of 0.15 V to -0.7 V. For the RRDE measurements, a potential of 0.3V was applied to ring electrode to obtain the ratio of ring to disk current.

The gas diffusion layer (GDL) was prepared from a mixture of activated carbon (Darco G-60A, Sigma Aldrich) and PTFE binder (60 wt% PTFE emulsion in water, Sigma Aldrich) at a weight ratio of 7 to 3.[107] Activated carbon and PTFE were first dispersed in DI-water. The two suspensions were then mixed in desired proportion ultrasonically for 1 h to form a homogeneous suspension. After filtering to remove water and drying at 60°C, a mixed powder was obtained. Proper amount of isopropyl alcohol was then added to the dried black powder to form slurry. GDL was manufactured via kneading and rolling process to control the thickness. Subsequently, a Ni-form was attached to

back side of the GDL as a current collector. The thickness of the GDL was kept at $\sim 350\ \mu\text{m}$ to ensure proper gas distribution and sufficient current collection in electrochemical testing. This GDL (without catalyst) was used as the baseline reference for comparison.

The air electrodes containing ORR catalysts were deposited on the GDL as follows: 2.0 mg catalyst powder was dispersed in 1 mL ethanol to form a homogeneous suspension. Then, 200 μL of the catalytic ink was transferred to the surface of the as-prepared GDL, which was subsequently dried at room temperature under vacuum for 0.5 h. To assemble a Zinc-air cell, 1 g of Zinc powder (Umicore) was used as the anode whereas Nylon net filters (Millipore) were used as the separator. 16-pi Air electrode was used as the cathode. Galvanodynamic experiments were carried out with a multichannel potentiostat (WBCS 3000, WonA Tech, Korea) at a wide range of current densities (0 to 340 mA/cm^2) to characterize the performance of the catalyst in a practical Zinc-air cell.

The materials structure, composition, morphology, and other properties were examined using an SEM (Nanonova 230, FEI) operating at 10kV, a TEM (JEOL JEM-2100F) operating at 200kV., an X-ray diffractometer (XRD, D/Max2000, Rigaku), an XPS (Thermo Fisher, UK), and a micro-Raman (WITec).

IV. RESULTS AND DISCUSSIONS

As schematically illustrated in **Figure 11**, a homogenous blend solution of polyacrylonitrile (PAN) and polystyrene (PS) dissolved in dimethylformamide (DMF) can be electrospun to nanofibers of tunable diameters. Upon stabilization at $400\ ^\circ\text{C}$ in air for 1 h, they can then be carbonized in N_2 atmosphere at different temperatures to form nitrogen-doped porous carbon nanofibers (NPCNFs).

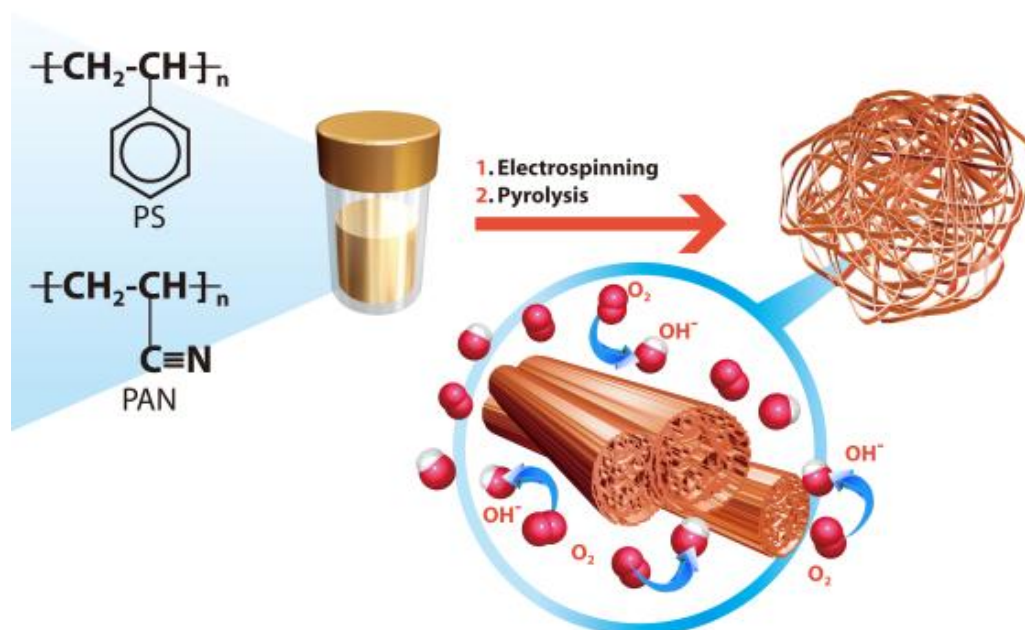


Figure 11. Polyacrylonitrile (PAN) and polystyrene (PS) were dissolved in dimethylformamide (DMF) as a carbon precursor. Nitrogen-doped porous carbon nanofibers were obtained after electrospinning and pyrolysis at 1100 °C to investigate the electrocatalytic activity for ORR

For brevity, the samples carbonized at 800, 900, 1000, and 1100 °C are denoted as NPCNFs-800, -900, -1000, and -1100, respectively. Nitrogen-containing polyacrylonitrile (PAN) precursor can introduce the nitrogen atoms on the carbon plane. Further, the carbon nano-fibers derived from PAN (without PS) using the sample fabrication process and carbonized at 1000 °C are denoted as CNF-1000. Under a scanning electron microscope (SEM), the NPCNFs-1100 sample has a nanofiber and churros-like morphology with diameters of 300 to 500 nm. Formation of the churros-like morphology is attributed to the carbonization of PS at >400 °C.[108] It is noted that the interconnected carbon nanofiber networks after carbonization (**Figure. 12**) offer a continuous pathway for efficient current collection.

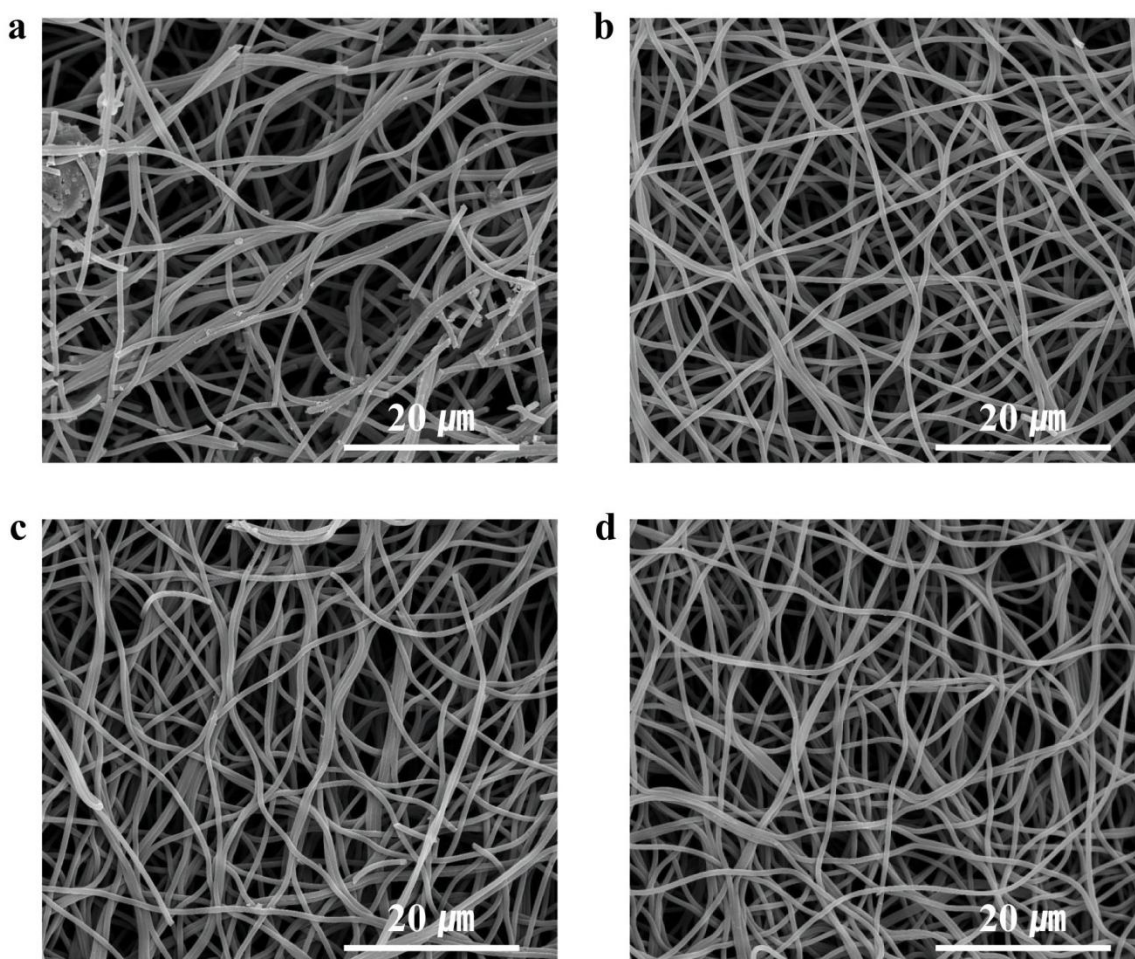


Figure 12. A typical SEM image of (a) NPCNFs-800, (b) NPCNFs-900, (c) NPCNFs-1000, (d) NPCNFs-1100. The interconnected carbon nanofiber webs of NPCNFs-1100 offer a continuous electron pathway to enhance efficient current collection.

Furthermore, transmission electron microscopy (TEM) and X-ray diffraction (XRD) analyses (**Figure 13** and **14**) suggest that the NPCNFs-1100 consisted of disordered carbon (hard carbon).[109, 110]

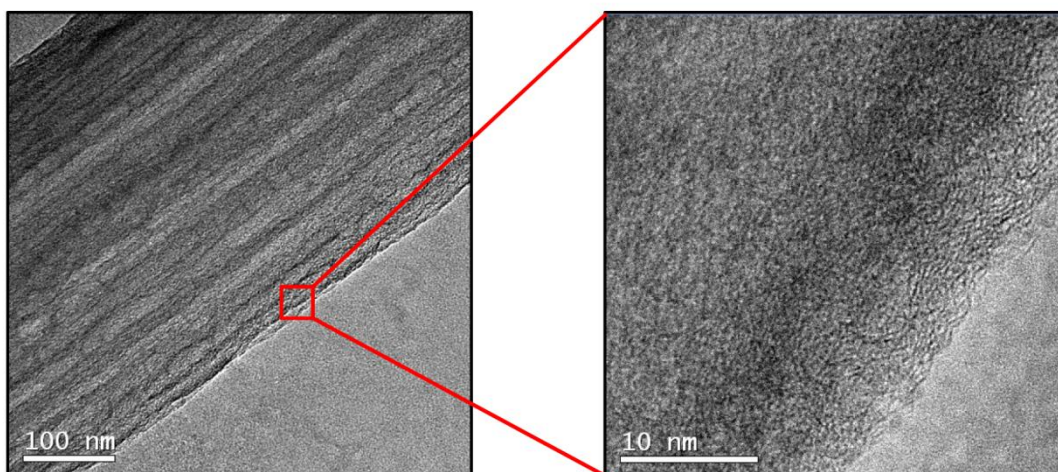


Figure 13. TEM images of a NPCNFs-1100 sample prepared from carbonization at 1100°C for 1h in nitrogen showing the porous structure.

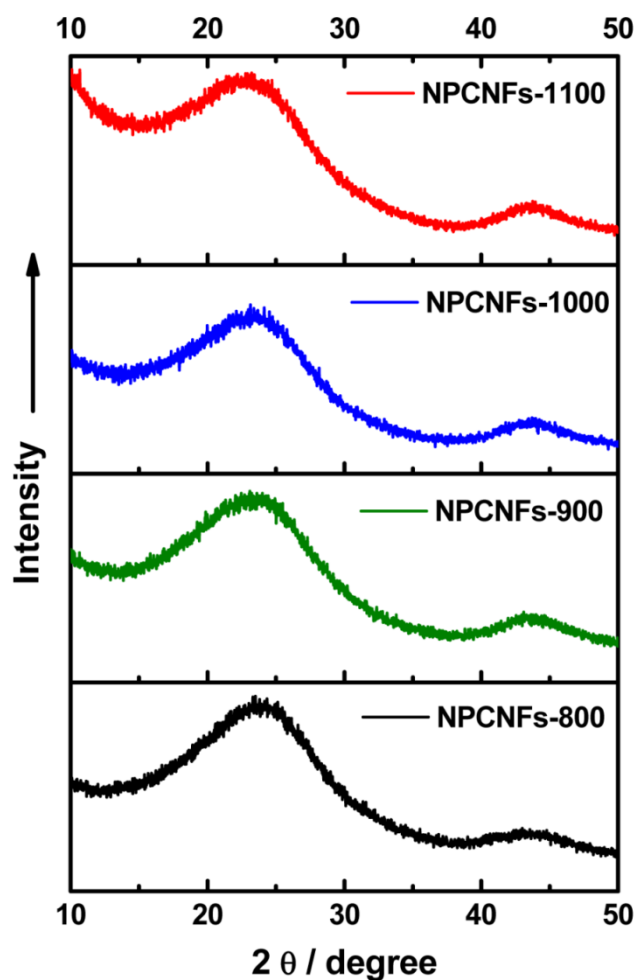


Figure 14. XRD patterns of NPCNFs carbonized at different temperatures (800°C to 1100°C). The patterns show that samples are composed of disordered carbon (hard carbon).

Pore size distribution was estimated from the adsorption data using the Barrett-Joyner-Halenda (BJH) model; the pore diameters are approximately 20 to 100 nm and the average pore volume is $\sim 0.74 \text{ cm}^3 \text{ g}^{-1}$. The NPCNFs a wide range pore size distribution, from mesopores (tens of nanometers)

to macropores (~110 nm), ideally suited for fast mass transport while maintaining high surface area (~1,271 m²g⁻¹). (Figure 15 and 16).

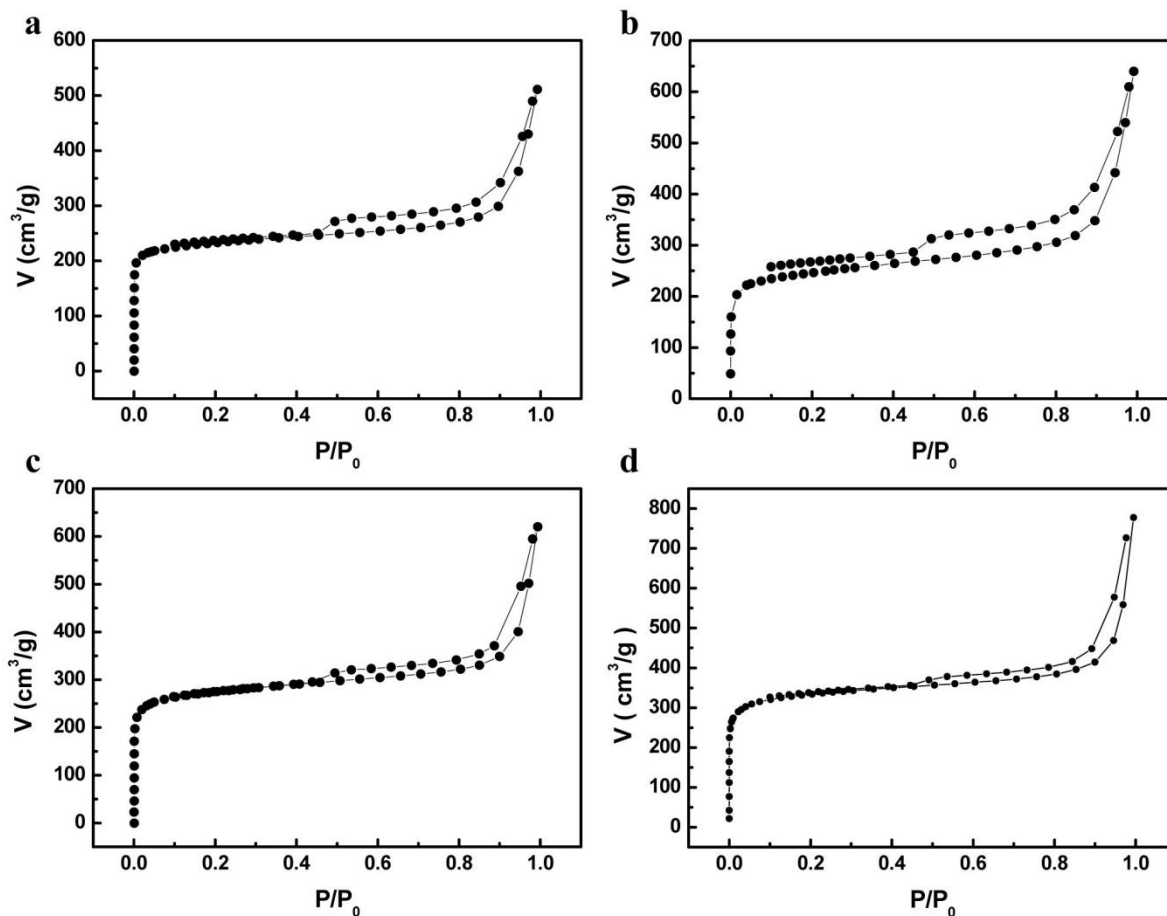


Figure 15. Nitrogen adsorption-desorption isotherm of (a) NPCNFs-800, (b) NPCNFs-900, (c) NPCNFs-1000, and (d) NPCNFs-1100 samples.

Samples	BET surface area (m ² ·g ⁻¹)	Average pore diameter (nm)	Total Pore volume (cm ³ ·g ⁻¹)
CNF-1000	747.03	1.80	0.34
NPCNFs-800	905.44	3.49	0.79
NPCNFs-900	914.32	4.33	0.99
NPCNFs-1000	1055.6	3.63	0.96
NPCNFs-1100	1271.2	3.78	1.21

Table 1. Physicochemical characterization of CNF-1000, NPCNFs-800, NPCNFs-900, NPCNFs-1000, and NPCNFs-1100.

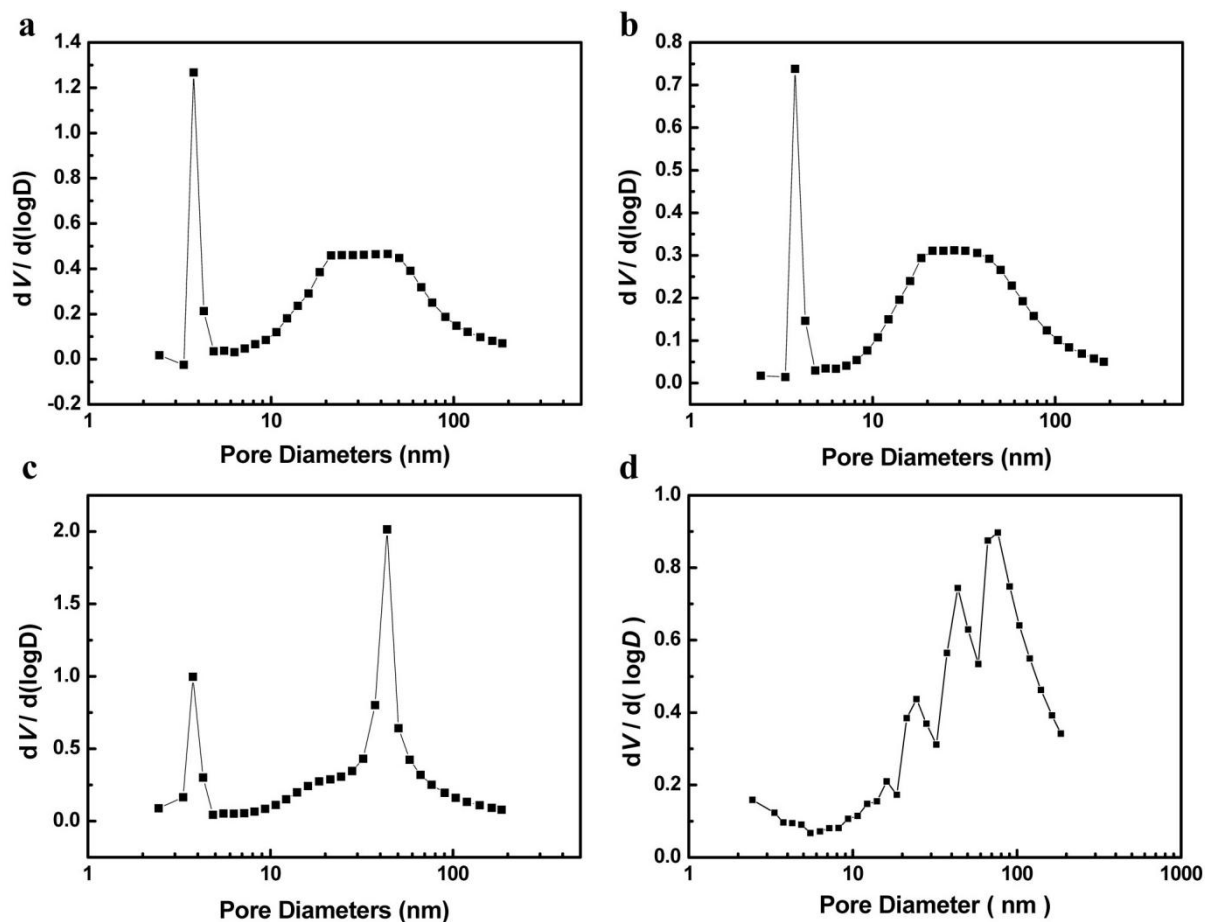


Figure 16. Pore size distribution of (a) NPCNFs-800, (b) NPCNFs-900, (c) NPCNFs-1000, and (d) NPCNFs-1100 samples.

Its surface area is the highest among all porous carbon nanofiber samples prepared from electrospinning of polymer solution (**Table 2**). Such an increase in surface area is expected to enhance electrochemical activity of the sample. Cyclic voltammograms collected for CNF-1000 and NPCNFs-1100 samples suggested that the electrochemically active surface area of the NPCNFs-1100 sample is approximately 2.5 times higher than that of the CNF-1000 sample (**Figure 17**). In addition, the electrical conductivities of the NPCNFs-1100 and the CNF-1000 samples were ~ 3.61 S/cm and ~ 1.76 S/cm, respectively (average value of measurements repeated by 10 times). Accordingly, the NPCNFs-1100 sample has large amount of pore volume that may facilitates fast transport of oxygen gas and aqueous electrolyte to the active sites.

Method	BET surface area (m ² ·g ⁻¹)	BJH pore size (nm)	BJH Pore volume (cm ³ ·g ⁻¹)	Morphology	Application	Refs
PAN/PMMA	940	11.89	0.82	Hollow	-	[85]
PAN/PVP	571	12.93	0.19	Porous	-	[86]
PAN/PS	-	~25	-	Porous	-	[111]
PAN/poly(AN-co-MMA)	321	100	0.36	Porous	-	[112]

Table 2. Characteristics of the PAN-based porous carbon nanofibers reported in previous studies.[85, 86, 111, 112]

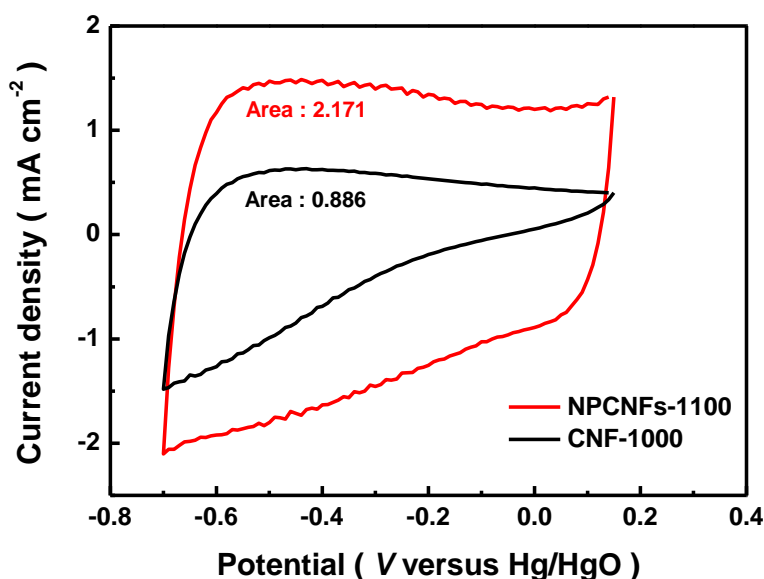


Figure 17. Cyclic voltammograms of NPCNFs-1100 and CNF-1000 samples obtained at a scan rate of 100mV/s in argon saturated 0.1 M KOH solution (stirring at 1600 rpm). The electrochemically active surface area (ECSA) of NPCNFs-1100 is approximately 2.5 times higher than CNF-1000.

While the active sites for ORR on nitrogen-doped carbon materials are still controversial, it is believed that the nitrogen groups play an essential role in the enhancement of ORR kinetics.[10, 113, 114] To correlate the ORR activity with the local atomistic structure of nitrogen, we carefully performed XPS analysis of the samples (**Figure 18**). The XPS spectra were deconvoluted to several different signals with binding energies of 398.0, 400.0, 401.3, and 402–405 eV corresponding to pyridinic N, pyrrolic N, graphitic N, and pyridinic N oxide, respectively[55, 115]. It is noted that spectral features of these peaks were significantly modified by the carbonization temperature. Previously, Matter et al. described the graphitic-N atoms at the edge sites are related to the binding energy of 401.3 eV,[9] which was also observed in the XPS spectra of our samples. Recent studies

concluded that graphitic-nitrogen enhanced the limiting current density due to the fact that N atoms reduce the electron density on the adjacent C nuclei, which facilitates electrons transfer from the adjacent C to N atoms and N backdonates electrons to adjacent C p_z orbitals.[7, 8, 116] For the NPCNF samples, the amount of the pyridinic type of nitrogen decreased whereas those of the pyrrolic- and the graphitic-like nitrogen increased with increasing annealing temperature (**Table 3** and **Figure 19**). The peak of pyridinic nitrogen was up-shifted to more graphitic nitrogen peak as the annealing temperature was increased. This is due to the fact that the thermally unstable pyridinic-nitrogen groups at high temperature are converted to pyrrolic-nitrogen and graphitic-nitrogen groups. This is consistent with a previous study.[7] Therefore, it is believed that an increase in pyrolysis temperature of the as-prepared samples leads to higher ORR activity. Moreover, the peak at 285.0 eV in the XPS spectra of C1s corresponds to graphitic sp^2 carbon, which is responsible for the electrical conductivity affecting ORR activity.[21]

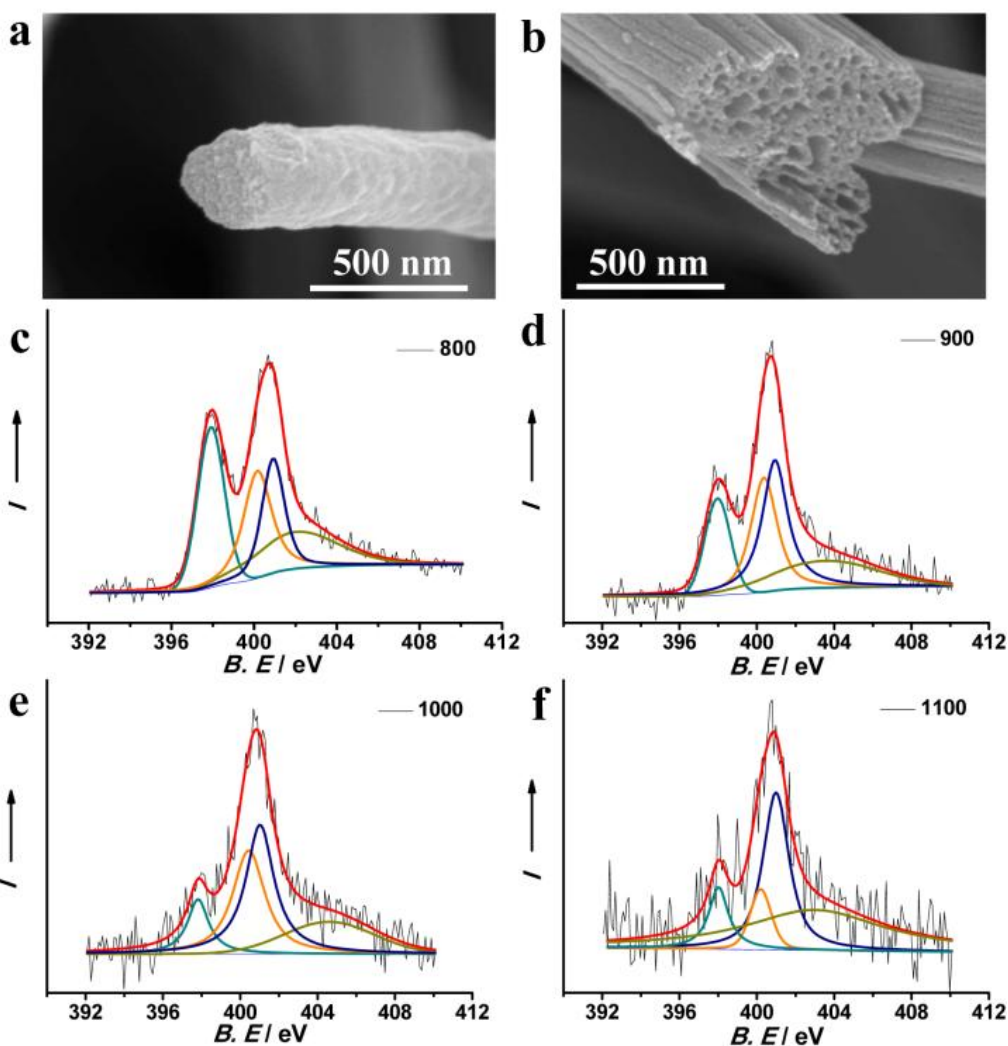


Figure 18. SEM images of a unmodified PAN based carbon fiber carbonized 1000 °C in N_2 atmosphere (CNF-1000). b Nitrogen-doped porous carbon nanofiber obtained via carbonized at 1100 °C in N_2 . The image shows formation of inner and outer pores consisting of meso- and micro- structures. The deconvoluted high-resolution N1s XPS spectra of c NPCNFs-800,

d NPCNFs-900, e NPCNFs-1000, and f NPCNFs-1100. These peaks were fitted mainly into four components centered at around 398.0, 400.0, 401.3, and 402-405 eV, corresponding to pyridinic N (Dark Cyan), pyrrolic N (Orange), graphitic N (Navy), and pyridinic N oxide (Olive), respectively

Samples	NPCNFs-800	NPCNFs-900	NPCNFs-1000	NPCNFs-1100
Nitrogen (at %)	5.88	4.66	2.96	2.2
Pyridinic-N	2.52	1.18	0.48	0.36
Pyrrolic-N	1.5	1.5	1	0.34
Graphitic-N	1.78	1.77	1.25	1.39
Pyridinic-N oxide	0.08	0.21	0.23	0.11

Table 3. Detailed breakdown of N 1s spectra from the NPCNFs samples from XPS analysis, indicating relative atomic ratios of N species.

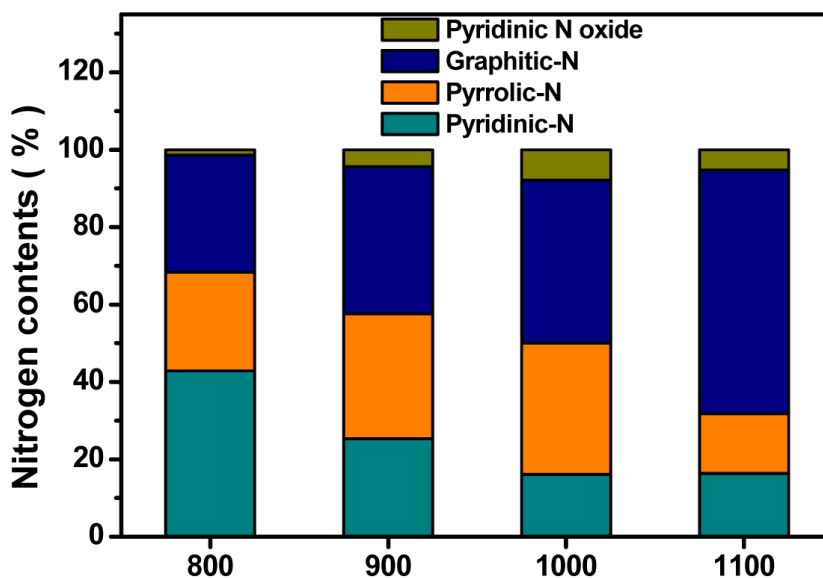


Figure 19. Converted values of N-species of each samples in Table S2.

Note that the half width of C1s peaks became narrower with increasing pyrolysis temperature, which can be ascribed to enhanced graphitization (**Figure 20**).[117] This result was further supported by the intensity ratio of the D to G bands observed at approximately 1310 cm^{-1} and 1583 cm^{-1} , respectively, in the Raman spectra (**Figure 21**), where the D band is attributed to amount of structural defects and G band is caused by the E_{2g} vibration mode of graphitic network.[118] The intensity ratio of D to G band (I_D/I_G) for NPCNFs-800, NPCNFs-900, NPCNFs-1000, and NPCNFs-1100 were 1.637, 1.556, 1.333, and 1.252, respectively. Clearly, the I_D/I_G decreased with increasing pyrolysis temperature, implying that the graphitic characteristics increased with pyrolysis temperature and so did the electrical conductivity.

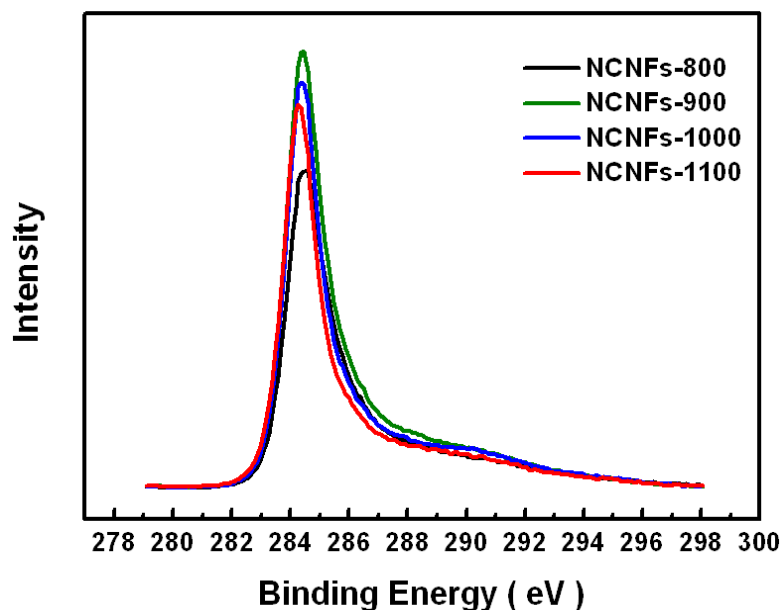


Figure 20. Some typical XPS spectra of C1s for NPCNFs.

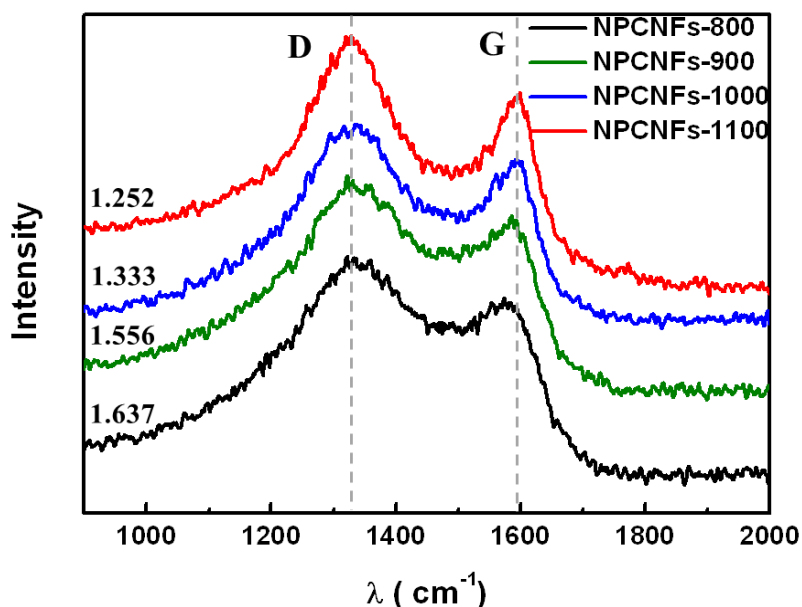


Figure 21. Raman spectra of NPCNFs after thermal treatment at different temperatures. The number adjacent to each spectrum represents the I_D/I_G ratio, which diminished with increasing pyrolysis temperature. Also, the G band became sharper with higher peak intensity at higher pyrolysis temperature.

We performed rotating-disk electrode (RDE) and rotating-ring-disk electrode (RRDE) experiments to characterize the electrocatalytic activities of CNF-1000 (as a control sample) and NPCNFs. Both RDE and RRDE voltammetry were performed in O_2 -saturated 0.1M KOH solution at a voltage scanning rate of 10 mVs^{-1} . The current densities of the air-electrode containing NPCNFs were increased with increasing rotation rate from 900 to 2500 rpm (Supplementary Fig. S9). As the pyrolysis temperature was increased from 800°C to 1100°C , the onset potentials were increased in the

more positive direction and finally reached about 0 V (vs. Hg/HgO), similar to the onset potential of a commercial Pt/C catalyst ($19.1 \mu\text{g}/\text{cm}^2$). To gain some insight into the ORR kinetics in a more quantitative manner, we analyzed the RDE and RRDE data using the Koutecky-Levich (K-L) equation. The average number of electrons transferred (n) in the electrode reaction was determined for the NPCNFs samples carbonized at 1100°C (Figure 22). With the RRDE technique, the electrocatalytic activity for ORR can be directly estimated from the ratio of disk to ring current. The amount of HO_2^- ion that usually recognized to be two-electrons pathway[4] affects low activity of ORR.

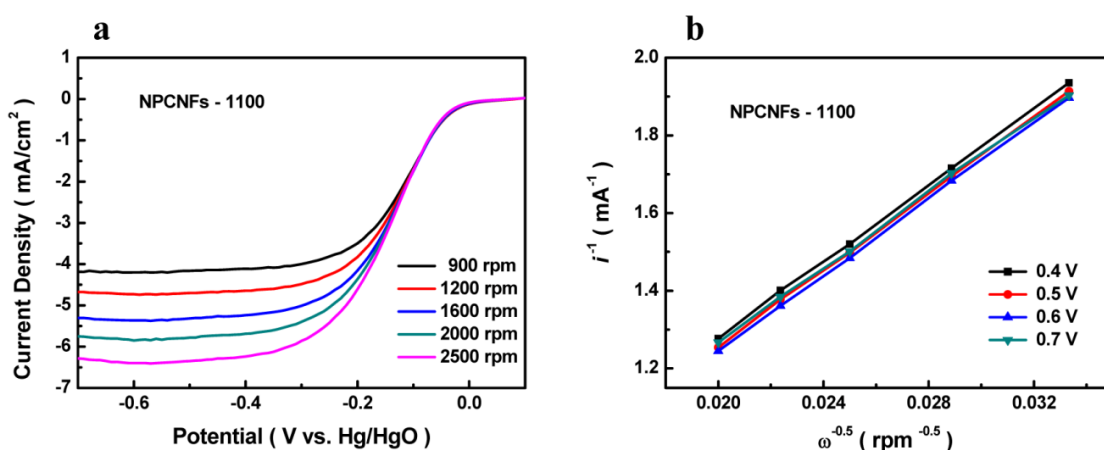


Figure 22. (a) Polarization curves of a NPCNFs-1100 sample in O₂-saturated 0.1M KOH electrolyte collected at different rotation rates at a scan rate of 10 mV/s, (b) Koutecky-Levich plots of the NPCNFs-1100 sample at potential -0.4, -0.5, -0.6, and -0.7 V vs. Hg/HgO.

As can be seen in **Figure 23b and 23d**, the amount of hydrogen peroxide that produced from the NPCNFs-1100 sample is similar to that of the commercial Pt/C catalyst ($19.1 \mu\text{g}/\text{cm}^2$) in the potential range of -0.2 V and -0.5 V (vs. Hg/HgO). In addition, the average number of electrons transferred for our best catalysts (NPCNFs-1100) was ~ 3.7 to 3.85 (close to 4) in the voltage range of -0.2 V to -0.5 V (vs. Hg/HgO), similar to that for the Pt/C sample, suggesting that it is an efficient 4-electron transfer process[119]. These results indicate that the composite samples are very promising electrocatalysts for ORR in an alkaline solution, demonstrating highly competitive performance but at a much lower cost than the benchmarked Pt/C catalysts. Moreover, the kinetic current density can be estimated using the Koutecky-Levich (K-L) equation.[4, 120] In a rotating disk electrode (RDE) measurement, the total current, j , can be described as,

$$\frac{1}{j} = \frac{1}{j_k} + \frac{1}{j_{dl}} = \frac{1}{j_k} + \frac{1}{B\omega^{0.5}} \quad (1)$$

$$j_k = nFkC_{O_2} \text{ (kinetic current)} \quad (2)$$

$$B = 0.2nFAC_{O_2}D_{O_2}^{2/3}\nu^{-1/6} \text{ (diffusion limiting current)} \quad (3)$$

where j_k is the kinetic current density, j_{dl} is diffusion limiting current density, n is the number of electrons transferred per O_2 molecular, F is the Faraday constant (96485 C/mol), A is the geometric area of the disk electrode ($7.06 \times 10^{-6} \text{ m}^2$), k is the rate constant (m/s) for the ORR, C_{O_2} is the saturated concentration of O_2 in solution (1.21 mol/m³ in 0.1 M KOH), D_{O_2} is the diffusion coefficient of O_2 in solution ($1.87 \times 10^{-9} \text{ m}^2/\text{s}$ in 0.10 M KOH), ν is the kinetic viscosity ($1 \times 10^{-6} \text{ m}^2/\text{s}$ in 0.1M KOH) and ω is the electrode rotation rate (rpm).

The percentage of peroxide ion and the number of electrons transferred (n) were determined from a rotating ring-disk electrode (RRDE) measurement as follows,

$$\text{HO}_2^- \text{ (}\%) = 200 \frac{\frac{I_r}{N}}{I_d + \frac{I_r}{N}} \quad (4)$$

$$n = 4 \frac{I_d}{I_d + \frac{I_r}{N}} \quad (5)$$

where I_d is the disk current, I_r is the ring current, and N is the current collection efficiency of the Pt ring, which was determined to be 0.41 from the reduction of $K_3Fe[CN]_6$.

Note that overall performance of CNF-1000 is similar to that of NPCNFs-800. On the other hand, the Pt catalyst with a one-step and four-electron pathway exhibits a kinetic current density of 7.48 mA/cm² at -0.15 V, which is similar to that of the NPCNFs-1100 (~6.87 mA/cm² at -0.15 V) but much higher than that of the NPCNFs-1000 (~2.91 mA/cm²) and NPCNFs-900 (0.68 mA/cm²) samples. The pyrolysis temperature critically affected the ORR activity because of its effect on the degree of graphitization and the nature or content of nitrogen doping. These results are consistent with the findings of Wang et al.; electrocatalytic activity depended not only on the surface area but also on the local atomistic structure of nitrogen.[121] The latter plays a greater role in enhancing ORR activity.[74]

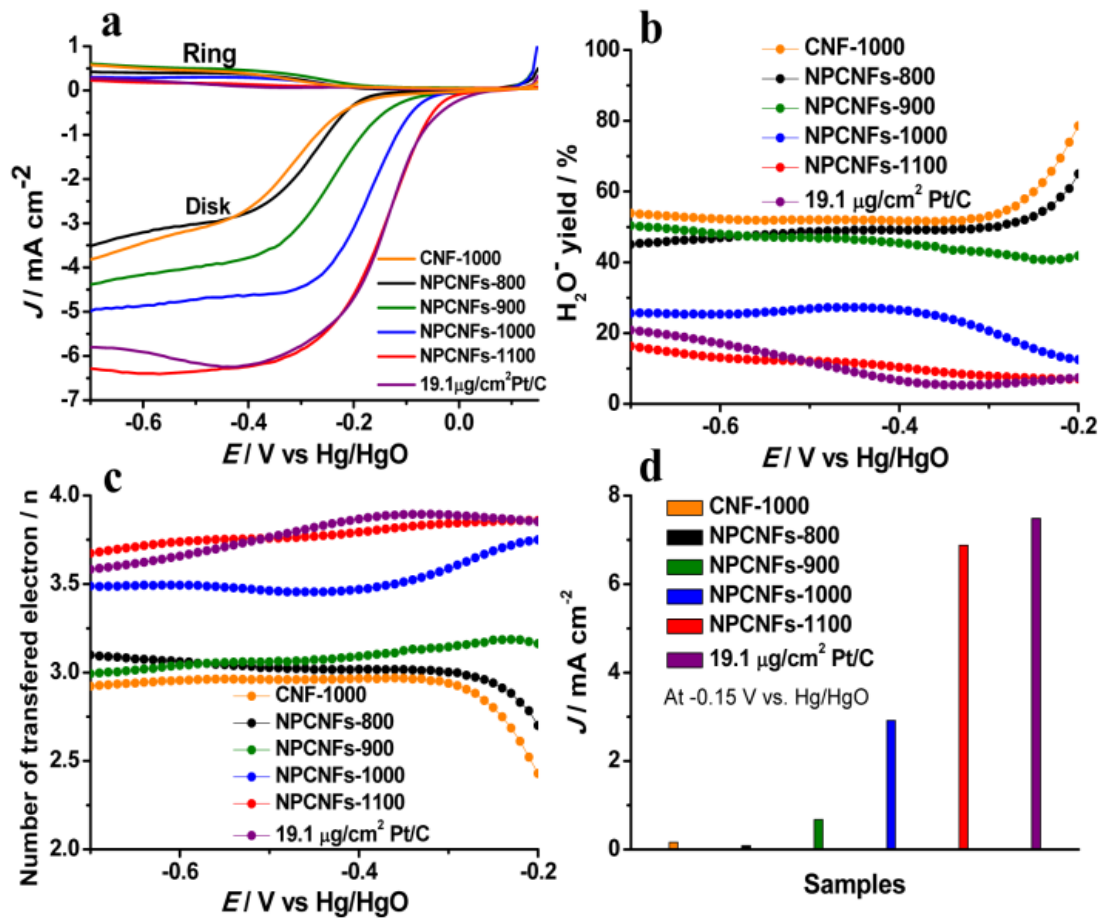


Figure 23. (a) Ring and disk current density in O_2 -saturated 0.1M KOH at a rotation rate of 2500 rpm. The disk potential was scanned at 10mV/s and the ring potential was kept constant at 0.3V (vs. Hg/HgO). (b) and (d) The number of electrons transferred and the percentage of peroxide at different potential range, respectively. (c) The kinetic-limiting current density at -0.15 V (vs. Hg/HgO).

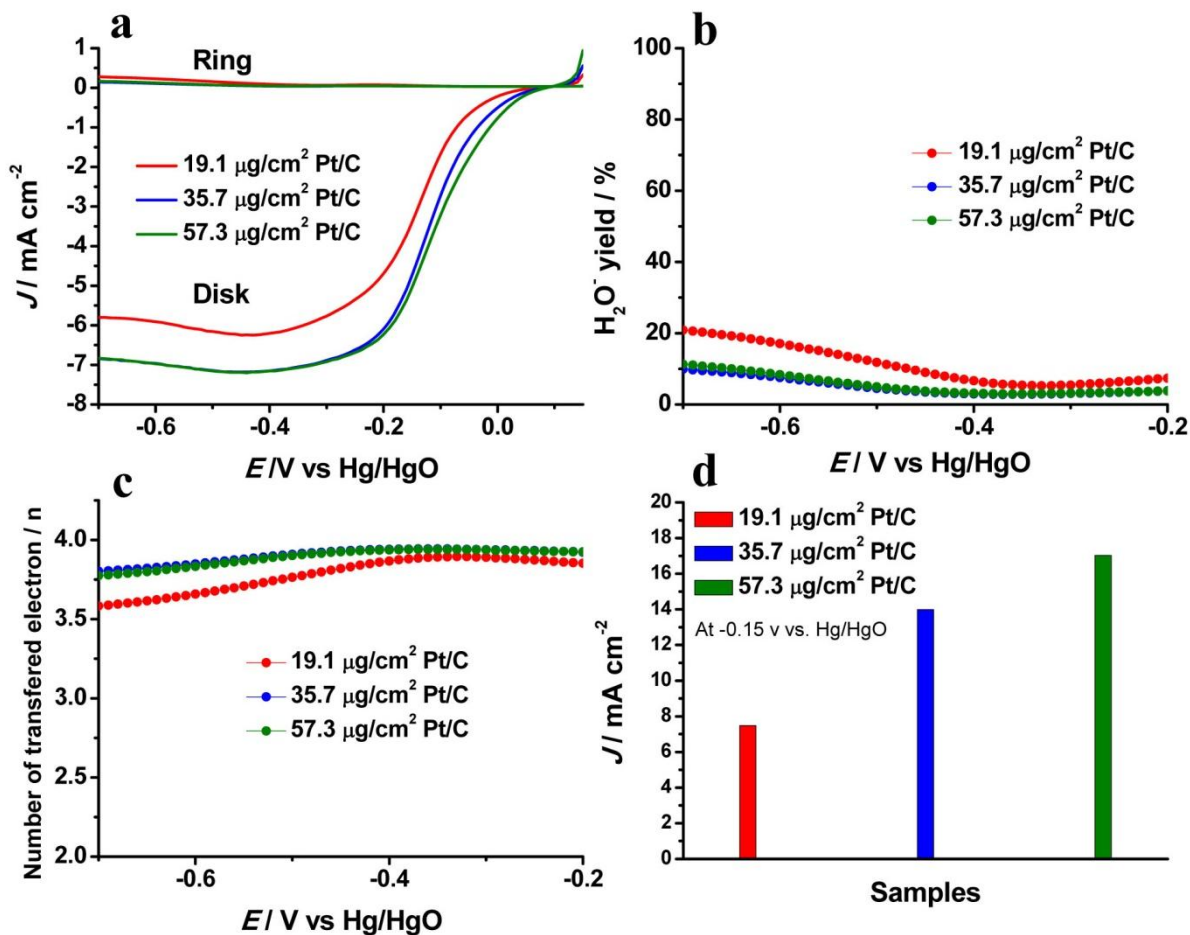


Figure 24. Electrochemical half-cell data of Pt/C catalysts. (a) Ring and disk current density in O_2 -saturated 0.1M KOH at a rotation rate of 2500 rpm. The disk potential was scanned at 10mV/s and the ring potential was kept constant at 0.3V (vs. Hg/HgO). (b) and (d) The number of electrons transferred and the percentage of peroxide at different potential range, respectively. (c) The kinetic-limiting current density at -0.15 V (vs. Hg/HgO).

Since durability is one of the major concerns in practical applications of batteries and fuel cells, the stability of NPCNFs-1100 was examined by measuring dimensional change of the redox peaks during cycling in a 0.1M KOH solution (**Figure 25**). The NPCNFs-1100 exhibited retention of 94% whereas the Pt/C showed retention of only 73% after 300 cycles. This result suggested that the stability of NPCNFs-1100 is much better than that of the commercial Pt/C catalyst.

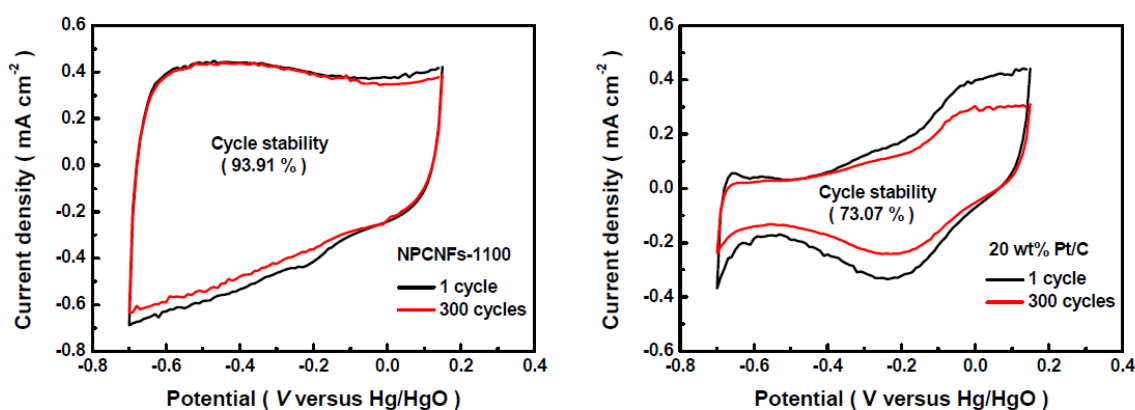


Figure 25. Cyclic voltammograms (the 1st and the 300th) of NPCNFs-1100 and 20 wt% Pt/C samples at a scan rate of 50 mV/s in argon saturated 0.1M KOH solution to show the stability during cycling.

The enhanced ORR activity of the NPCNFs-1100 catalyst was further evaluated in a Zn-air cell using an aqueous 6M KOH solution as the electrolyte. As illustrated in **Figure 26a**, the Zn-air cell was composed of an air cathode, a separator, and a zinc powder anode. The air cathode consisted of a gas diffusion layer (GDL) and a catalyst layer (e.g., NPCNFs-1100 or Pt/C catalysts). The current densities of the test cells were varied from 0 to 340 mA/cm², demonstrating peak power densities of 194 mW/cm² for the cell with a NPCNFs-1100 catalyst and 192 mW/cm² for that with the Pt/C catalyst. As depicted in **Figure 26c**, even though there was a relatively small potential difference between the cell with the NPCNFs-1100 catalyst and the one with the Pt/C catalyst at low current densities, similar I-V characteristics were observed for both at current densities greater than 180 mA/cm². This result suggests that the NPCNFs-1100 catalyst is comparable to the commercial Pt/C catalyst in performance but the former is much less expensive than the latter.

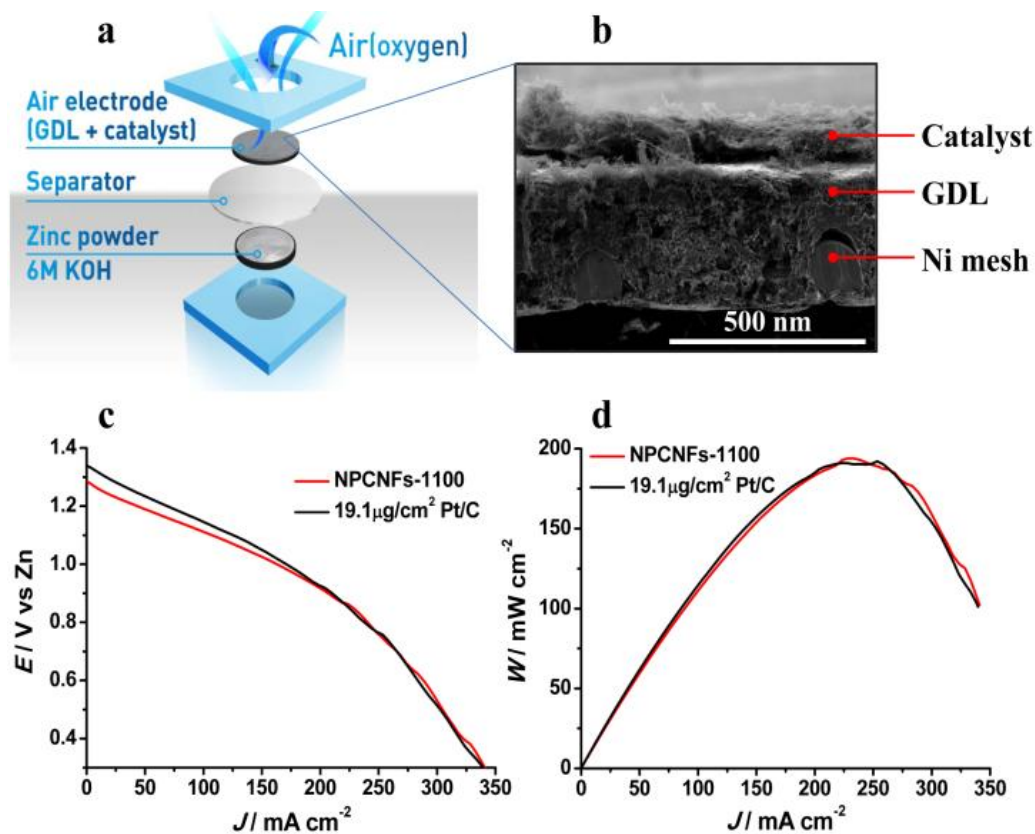


Figure 26. (a) a zinc-air cell consisted of an air cathode, a separator, and a zinc powder anode with 6M KOH. (b) the air electrode divided into gas diffusion layer (GDL), catalyst layer(NPCNFs-1100), and Ni mesh as a current collector. (c) polarization curve with a scan rate of 5 mA/cm²-sec and d corresponding power density curves at a constant current density varied from 0 to 340 mA/cm².

It is also noted that this power density is similar to that demonstrated in a Zn-Air cell with Ketjenblack carbon supported MnO_x nanowires, although the cell configurations used in the two cases are different (a single catalytic layer of MnO_x/C vs a cathode consisting of two layers: a gas diffusion layer and a catalytic layer of NPCNFs).

V. CONCLUSIONS

we have developed a simple and cost-effective process for fabrication of nitrogen-doped highly porous carbon nanofibers with diameters of 300 to 500 nm via electrospinning of PAN/PS blend followed by carbonization at high temperatures. The ORR activity of the nitrogen-doped carbon nanofibers depended strongly on the carbonization temperature, which determines the nature and amount of nitrogen doping. Graphitic structures and high specific surface areas formed at higher temperatures enhanced electrical conductivity and ORR activity while facilitating fast mass transport through porous electrodes. Also, the local atomistic structures of nitrogen functional groups play a key role in altering the ORR activity. The pyrrolic-N and graphitic-N at the edge carbon planes appear to be beneficial to enhancing ORR activity. The NPCNFs catalyst prepared at 1100°C showed the highest ORR activity with one-step and quasi-four-electron transfer pathway. Further and in particular, a Zn-air battery based on the NPCNFs catalyst demonstrated comparable power density to that based on a commercial Pt/C catalyst.

VI. Acknowledgements

2 년동안 가르쳐 주시고 이끌어 주신 조재필 교수님께 우선 감사 드립니다.

저의 사수로써 어려움이 있을 때 항상 도와주신 이장수, 김선태 형에게도 고마움을 전합니다. 석사동기이면서 많은 가르침을 주신 정성원 형님, 가깝지만 먼 곳에서 근무하시는 조용현 형님, 우리 실험실을 이끌어 주신 이상한 형 결혼 축하드려요, 함께 쏘렌토 가지 못해 미안해요 정수경 형, 졸업하시면 꼭 우리 회사로 와요 노미정 누나, 실험 아이디어도 많았고 공유도 많이 해준 나쁜남자 손윤국 형, 실험적인 측면이나 생활적인 면에서 많은 도움을 준 오필건 형, 곧 수염깎고 머리밀고 군대갈 고민성 형 꼭 전역하면 네이처 쓰세요, 전형적 유부남인 조민기 형, 꼭 올해안에 장가가길 빌어요 이민준 형, 짧지만 굵은 인연 이래은 누나, 내 옆자리를 굳건히 지켜준 박미희 양, 졸업해서 포닥 꼭 가야돼 김혜정 양, 실험실 일이라면 앞서서 진행했던 고마운 심수진 양, 서울이 고향이 아닌 것 같은 박민준 군, 내년에 꼭 졸업해 정민슬 양, 얼굴 큰 손영욱 군, 전기방사 대가가 될 박주혁 군, 먹보 남규태 군, 몸짱 명승준 군, 홍일점 남해슬 양.

그리고 마지막으로 항상 옆에서 비가 오나 눈이 오나 힘이 되어준 김지은 양.

다들 짧은 인연이지만 졸업해서도 계속 연락하면서 인연을 이어갔으면 합니다.

VII. REFERENCES

1. Lee, J.-S., et al., *Ionic liquid modified graphene nanosheets anchoring manganese oxide nanoparticles as efficient electrocatalysts for Zn-air batteries*. Energy & Environmental Science, 2011. **4**(10): p. 4148-4154.
2. Lee, J.S., et al., *Metal-Air Batteries with High Energy Density: Li-Air versus Zn-Air*. Advanced Energy Materials, 2011. **1**(1): p. 34-50.
3. Debe, M.K., *Electrocatalyst approaches and challenges for automotive fuel cells*. Nature, 2012. **486**(7401): p. 43-51.
4. Paulus, U.A., et al., *Oxygen reduction on a high-surface area Pt/Vulcan carbon catalyst: a thin-film rotating ring-disk electrode study*. Journal of Electroanalytical Chemistry, 2001. **495**(2): p. 134-145.
5. Stamenkovic, V.R., et al., *Improved Oxygen Reduction Activity on Pt₃Ni(111) via Increased Surface Site Availability*. Science, 2007: p. 1135941.
6. Gasteiger, H.A., et al., *Activity benchmarks and requirements for Pt, Pt-alloy, and non-Pt oxygen reduction catalysts for PEMFCs*. Applied Catalysis B-Environmental, 2005. **56**(1-2): p. 9-35.
7. Lai, L.F., et al., *Exploration of the active center structure of nitrogen-doped graphene-based catalysts for oxygen reduction reaction*. Energy & Environmental Science, 2012. **5**(7): p. 7936-7942.
8. Geng, D.S., et al., *High oxygen-reduction activity and durability of nitrogen-doped graphene*. Energy & Environmental Science, 2011. **4**(3): p. 760-764.
9. Matter, P.H., L. Zhang, and U.S. Ozkan, *The role of nanostructure in nitrogen-containing carbon catalysts for the oxygen reduction reaction*. Journal of Catalysis, 2006. **239**(1): p. 83-96.
10. Gong, K., et al., *Nitrogen-Doped Carbon Nanotube Arrays with High Electrocatalytic Activity for Oxygen Reduction*. Science, 2009. **323**(5915): p. 760-764.
11. Ozaki, J.-i., et al., *Enhancement of oxygen reduction activity by carbonization of furan resin in the presence of phthalocyanines*. Carbon, 2006. **44**(7): p. 1324-1326.
12. Ozaki, J.-i., et al., *Simultaneous doping of boron and nitrogen into a carbon to enhance its oxygen reduction activity in proton exchange membrane fuel cells*. Carbon, 2006. **44**(15): p. 3358-3361.
13. Ozaki, J.-i., et al., *Preparation and oxygen reduction activity of BN-doped carbons*. Carbon, 2007. **45**(9): p. 1847-1853.
14. Matter, P.H., et al., *Oxygen Reduction Reaction Catalysts Prepared from Acetonitrile Pyrolysis over Alumina-Supported Metal Particles*. The Journal of Physical Chemistry B, 2006. **110**(37): p. 18374-18384.
15. Wang, Y., et al., *Nitrogen-Doped Graphene and Its Application in Electrochemical Biosensing*. ACS Nano, 2010. **4**(4): p. 1790-1798.
16. Qu, L., et al., *Nitrogen-Doped Graphene as Efficient Metal-Free Electrocatalyst for Oxygen Reduction in Fuel Cells*. ACS Nano, 2010. **4**(3): p. 1321-1326.
17. Wang, X., et al., *N-Doping of Graphene Through Electrothermal Reactions with Ammonia*. Science, 2009. **324**(5928): p. 768-771.
18. Sumpter, B.G., et al., *Nitrogen-mediated carbon nanotube growth: Diameter reduction, metallicity, bundle dispersability, and bamboo-like structure formation*. ACS Nano, 2007. **1**(4): p. 369-375.
19. Wang, X.R., et al., *N-Doping of Graphene Through Electrothermal Reactions with Ammonia*. Science, 2009. **324**(5928): p. 768-771.
20. Li, D. and Y.N. Xia, *Electrospinning of nanofibers: Reinventing the wheel?* Advanced Materials, 2004. **16**(14): p. 1151-1170.
21. Inagaki, M., Y. Yang, and F. Kang, *Carbon nanofibers prepared via electrospinning*. Adv Mater, 2012. **24**(19): p. 2547-66.
22. Bognitzki, M., et al., *Nanostructured fibers via electrospinning*. Advanced Materials, 2001.

- 13(1): p. 70-72.
23. Huang, Z.M., et al., *A review on polymer nanofibers by electrospinning and their applications in nanocomposites*. Composites Science and Technology, 2003. **63**(15): p. 2223-2253.
 24. Yuan, J.Y., et al., *Nitrogen-doped carbon fibers and membranes by carbonization of electrospun poly(ionic liquid)s*. Polymer Chemistry, 2011. **2**(8): p. 1654-1657.
 25. Qiu, Y., et al., *Nitrogen-doped ultrathin carbon nanofibers derived from electrospinning: Large-scale production, unique structure, and application as electrocatalysts for oxygen reduction*. Journal of Power Sources, 2011. **196**(23): p. 9862-9867.
 26. Zhu, W.H., et al., *New structures of thin air cathodes for zinc–air batteries*. Journal of Applied Electrochemistry, 2003. **33**(1): p. 29-36.
 27. Dirkse, T.P. and D.J. Kroon, *Effect of ionic strength on the passivation of zinc electrodes in KOH solutions*. Journal of Applied Electrochemistry, 1971. **1**(4): p. 293-296.
 28. Sapkota, P. and H. Kim, *Zinc–air fuel cell, a potential candidate for alternative energy*. Journal of Industrial and Engineering Chemistry, 2009. **15**(4): p. 445-450.
 29. Müller, S., K. Striebel, and O. Haas, *La_{0.6}Ca_{0.4}CoO₃: a stable and powerful catalyst for bifunctional air electrodes*. Electrochimica Acta, 1994. **39**(11–12): p. 1661-1668.
 30. Kim Jee Hoon, E.S.W., Moon Seong In, Yun Mun Soo, Kim Ju Yong, Yug Gyeong Chang, Park Jeong Hoo *Effects of PTFE Contents on Characteristics of Cathode for Zn Air Batteries* Journal of the Korean Electrochemical Society 2003. **6**: p. 203-207.
 31. Fang, Z.-q., et al., *Preparation and electrochemical property of three-phase gas-diffusion oxygen electrodes for metal air battery*. Electrochimica Acta, 2006. **51**(26): p. 5654-5659.
 32. Xie, F., et al., *Increasing the three-phase boundary by a novel three-dimensional electrode*. Journal of Power Sources, 2005. **141**(2): p. 211-215.
 33. Yang, C.-C., *Preparation and characterization of electrochemical properties of air cathode electrode*. International Journal of Hydrogen Energy, 2004. **29**(2): p. 135-143.
 34. Furuya, N., *A new method of making a gas diffusion electrode*. Journal of Solid State Electrochemistry, 2003. **8**(1): p. 48-50.
 35. Eom, S.-W., et al., *The roles and electrochemical characterizations of activated carbon in zinc air battery cathodes*. Electrochimica Acta, 2006. **52**(4): p. 1592-1595.
 36. Fierro, C., et al., *In situ mossbauer effect spectroscopy of a model iron perovskite electrocatalyst*. Electrochimica Acta, 1988. **33**(7): p. 941-945.
 37. Jörissen, L., *Bifunctional oxygen/air electrodes*. Journal of Power Sources, 2006. **155**(1): p. 23-32.
 38. Ross, P.N. and M. Sattler, *The Corrosion of Carbon Black Anodes in Alkaline Electrolyte*. Journal of the Electrochemical Society, 1988. **135**(6): p. 1464-1470.
 39. Neburchilov, V., et al., *A review on air cathodes for zinc–air fuel cells*. Journal of Power Sources, 2010. **195**(5): p. 1271-1291.
 40. Santos, E. and W. Schmickler, *d-Band Catalysis in Electrochemistry*. ChemPhysChem, 2006. **7**(11): p. 2282-2285.
 41. Hammer, B. and J.K. Nørskov, *Why gold is the noblest of all the metals*. Nature, 1995. **376**(6537): p. 238-240.
 42. Nørskov, J.K., et al., *Origin of the Overpotential for Oxygen Reduction at a Fuel-Cell Cathode*. The Journal of Physical Chemistry B, 2004. **108**(46): p. 17886-17892.
 43. Greeley, J., J.K. Nørskov, and M. Mavrikakis, *ELECTRONIC STRUCTURE AND CATALYSIS ON METAL SURFACES*. Annual Review of Physical Chemistry, 2002. **53**(1): p. 319-348.
 44. Lee, K., M. Kim, and H. Kim, *Catalytic nanoparticles being facet-controlled*. Journal of Materials Chemistry, 2010. **20**(19): p. 3791-3798.
 45. Greeley, J., et al., *Alloys of platinum and early transition metals as oxygen reduction electrocatalysts*. Nat Chem, 2009. **1**(7): p. 552-556.
 46. Zhang, J., et al., *Controlling the Catalytic Activity of Platinum-Monolayer Electrocatalysts for Oxygen Reduction with Different Substrates*. Angewandte Chemie, 2005. **117**(14): p. 2170-2173.
 47. Yu, T.H., et al., *Improved Non-Pt Alloys for the Oxygen Reduction Reaction at Fuel Cell*

- Cathodes Predicted from Quantum Mechanics*. The Journal of Physical Chemistry C, 2010. **114**(26): p. 11527-11533.
48. Gasteiger, H.A., et al., *Activity benchmarks and requirements for Pt, Pt-alloy, and non-Pt oxygen reduction catalysts for PEMFCs*. Applied Catalysis B: Environmental, 2005. **56**(1–2): p. 9-35.
 49. Ma, Y. and P.B. Balbuena, *Designing oxygen reduction catalysts: Insights from metalloenzymes*. Chemical Physics Letters, 2007. **440**(1–3): p. 130-133.
 50. Hamdani, M., R.N. Singh, and P. Chartier, *Co₃O₄ and Co- Based Spinel Oxides Bifunctional Oxygen Electrodes*. International Journal of Electrochemical Science, 2010. **5**(4): p. 556-577.
 51. Nikolova, V., et al., *Electrocatalysts for bifunctional oxygen/air electrodes*. Journal of Power Sources, 2008. **185**(2): p. 727-733.
 52. Wang, B., *Recent development of non-platinum catalysts for oxygen reduction reaction*. Journal of Power Sources, 2005. **152**(0): p. 1-15.
 53. Gorlin, Y. and T.F. Jaramillo, *A Bifunctional Nonprecious Metal Catalyst for Oxygen Reduction and Water Oxidation*. Journal of the American Chemical Society, 2010. **132**(39): p. 13612-13614.
 54. Han, J.-J., N. Li, and T.-Y. Zhang, *Ag/C nanoparticles as an cathode catalyst for a zinc-air battery with a flowing alkaline electrolyte*. Journal of Power Sources, 2009. **193**(2): p. 885-889.
 55. Pels, J.R., et al., *Evolution of nitrogen functionalities in carbonaceous materials during pyrolysis*. Carbon, 1995. **33**(11): p. 1641-1653.
 56. Stańczyk, K., et al., *Transformation of nitrogen structures in carbonization of model compounds determined by XPS*. Carbon, 1995. **33**(10): p. 1383-1392.
 57. Buckley, A.N., *Nitrogen functionality in coals and coal-tar pitch determined by X-ray photoelectron spectroscopy*. Fuel Processing Technology, 1994. **38**(3): p. 165-179.
 58. Montoya, A., F. Mondragón, and T.N. Truong, *Kinetics of nitric oxide desorption from carbonaceous surfaces*. Fuel Processing Technology, 2002. **77–78**(0): p. 453-458.
 59. Côté, R., et al., *Influence of nitrogen-containing precursors on the electrocatalytic activity of heat-treated Fe(OH)₂ on carbon black for O₂ reduction*. Journal of the Electrochemical Society, 1998. **145**(7): p. 2411-2418.
 60. Casanovas, J., et al., *Origin of the large N 1s binding energy in X-ray photoelectron spectra of calcined carbonaceous materials*. Journal of the American Chemical Society, 1996. **118**(34): p. 8071-8076.
 61. Darrell, H.R. and C. Iksoo, *Nanometre diameter fibres of polymer, produced by electrospinning*. Nanotechnology, 1996. **7**(3): p. 216.
 62. Frenot, A. and I.S. Chronakis, *Polymer nanofibers assembled by electrospinning*. Current Opinion in Colloid & Interface Science, 2003. **8**(1): p. 64-75.
 63. Huang, Z.-M., et al., *A review on polymer nanofibers by electrospinning and their applications in nanocomposites*. Composites Science and Technology, 2003. **63**(15): p. 2223-2253.
 64. Kessick, R., J. Fenn, and G. Tepper, *The use of AC potentials in electro spraying and electrospinning processes*. Polymer, 2004. **45**(9): p. 2981-2984.
 65. Reneker, D.H., et al., *Bending instability of electrically charged liquid jets of polymer solutions in electrospinning*. Journal of Applied Physics, 2000. **87**(9): p. 4531-4547.
 66. Shin, Y.M., et al., *Electrospinning: A whipping fluid jet generates submicron polymer fibers*. Applied Physics Letters, 2001. **78**(8): p. 1149-1151.
 67. Yarin, A.L., S. Koombhongse, and D.H. Reneker, *Taylor cone and jetting from liquid droplets in electrospinning of nanofibers*. Journal of Applied Physics, 2001. **90**(9): p. 4836-4846.
 68. Shin, Y.M., et al., *Experimental characterization of electrospinning: the electrically forced jet and instabilities*. Polymer, 2001. **42**(25): p. 09955-09967.
 69. Hohman, M.M., et al., *Electrospinning and electrically forced jets. I. Stability theory*. Physics of Fluids, 2001. **13**(8): p. 2201-2220.
 70. Hohman, M.M., et al., *Electrospinning and electrically forced jets. II. Applications*. Physics

- of Fluids, 2001. **13**(8): p. 2221-2236.
71. Fridrikh, S.V., et al., *Controlling the Fiber Diameter during Electrospinning*. Physical Review Letters, 2003. **90**(14): p. 144502.
 72. Feng, J.J., *The stretching of an electrified non-Newtonian jet: A model for electrospinning*. Physics of Fluids, 2002. **14**(11): p. 3912-3926.
 73. Feng, J.J., *Stretching of a straight electrically charged viscoelastic jet*. Journal of Non-Newtonian Fluid Mechanics, 2003. **116**(1): p. 55-70.
 74. Li, Y.G., et al., *An oxygen reduction electrocatalyst based on carbon nanotube-graphene complexes*. Nature Nanotechnology, 2012. **7**(6): p. 394-400.
 75. Wang, Y., S. Serrano, and J.J. Santiago-Aviles, *Conductivity measurement of electrospun PAN-based carbon nanofiber*. Journal of Materials Science Letters, 2002. **21**(13): p. 1055-1057.
 76. Wang, Y., S. Serrano, and J.J. Santiago-Avilés, *Raman characterization of carbon nanofibers prepared using electrospinning*. Synthetic Metals, 2003. **138**(3): p. 423-427.
 77. Wang, Y. and J.J. Santiago-Aviles, *Large negative magnetoresistance and two-dimensional weak localization in carbon nanofiber fabricated using electrospinning*. Journal of Applied Physics, 2003. **94**(3): p. 1721-1727.
 78. Zussman, E., et al., *Mechanical and structural characterization of electrospun PAN-derived carbon nanofibers*. Carbon, 2005. **43**(10): p. 2175-2185.
 79. Zhou, Z., et al., *Development of carbon nanofibers from aligned electrospun polyacrylonitrile nanofiber bundles and characterization of their microstructural, electrical, and mechanical properties*. Polymer, 2009. **50**(13): p. 2999-3006.
 80. Sabina, P., Z. Eyal, and C. Yachin, *The effect of embedded carbon nanotubes on the morphological evolution during the carbonization of poly(acrylonitrile) nanofibers*. Nanotechnology, 2008. **19**(16): p. 165603.
 81. Prilutsky, S., E. Zussman, and Y. Cohen, *Carbonization of electrospun poly(acrylonitrile) nanofibers containing multiwalled carbon nanotubes observed by transmission electron microscope with in situ heating*. Journal of Polymer Science Part B: Polymer Physics, 2010. **48**(20): p. 2121-2128.
 82. Shim, W.G., et al., *Adsorption characteristics of benzene on electrospun-derived porous carbon nanofibers*. Journal of Applied Polymer Science, 2006. **102**(3): p. 2454-2462.
 83. Nataraj, S.K., K.S. Yang, and T.M. Aminabhavi, *Polyacrylonitrile-based nanofibers—A state-of-the-art review*. Progress in Polymer Science, 2012. **37**(3): p. 487-513.
 84. Zussman, E., et al., *Electrospun Polyaniline/Poly(methyl methacrylate)-Derived Turbostratic Carbon Micro-/Nanotubes*. Advanced Materials, 2006. **18**(3): p. 348-353.
 85. Kim, C., et al., *Synthesis and Characterization of Porous Carbon Nanofibers with Hollow Cores Through the Thermal Treatment of Electrospun Copolymeric Nanofiber Webs*. Small, 2007. **3**(1): p. 91-95.
 86. Zhang, Z., et al., *Polyacrylonitrile and Carbon Nanofibers with Controllable Nanoporous Structures by Electrospinning*. Macromolecular Materials and Engineering, 2009. **294**(10): p. 673-678.
 87. Niu, H., et al., *Preparation, structure and supercapacitance of bonded carbon nanofiber electrode materials*. Carbon, 2011. **49**(7): p. 2380-2388.
 88. Park, S.H., et al., *Preparations of pitch-based CF/ACF webs by electrospinning*. Carbon, 2003. **41**(13): p. 2655-2657.
 89. Park, S.H., C. Kim, and K.S. Yang, *Preparation of carbonized fiber web from electrospinning of isotropic pitch*. Synthetic Metals, 2004. **143**(2): p. 175-179.
 90. Bui, N.-N., et al., *Activated carbon fibers from electrospinning of polyacrylonitrile/pitch blends*. Carbon, 2009. **47**(10): p. 2538-2539.
 91. Rose, M., et al., *High surface area carbide-derived carbon fibers produced by electrospinning of polycarbosilane precursors*. Carbon, 2010. **48**(2): p. 403-407.
 92. Yang, K.S., et al., *Preparation of carbon fiber web from electrostatic spinning of PMDA-ODA poly(amic acid) solution*. Carbon, 2003. **41**(11): p. 2039-2046.
 93. Kim, C., et al., *Supercapacitor performances of activated carbon fiber webs prepared by*

- electrospinning of PMDA-ODA poly(amic acid) solutions*. *Electrochimica Acta*, 2004. **50**(2–3): p. 883-887.
94. Chung, G.S., S.M. Jo, and B.C. Kim, *Properties of carbon nanofibers prepared from electrospun polyimide*. *Journal of Applied Polymer Science*, 2005. **97**(1): p. 165-170.
 95. Xuyen, N.T., et al., *Enhancement of Conductivity by Diameter Control of Polyimide-Based Electrospun Carbon Nanofibers*. *The Journal of Physical Chemistry B*, 2007. **111**(39): p. 11350-11353.
 96. Kim, C., et al., *Fabrications and structural characterization of ultra-fine carbon fibres by electrospinning of polymer blends*. *Solid State Communications*, 2007. **142**(1–2): p. 20-23.
 97. Yang, Y., et al., *Highly porous electrospun polyvinylidene fluoride (PVDF)-based carbon fiber*. *Carbon*, 2011. **49**(11): p. 3395-3403.
 98. Wang, M.-X., et al., *Porous carbon nanofibers with narrow pore size distribution from electrospun phenolic resins*. *Materials Letters*, 2011. **65**(12): p. 1875-1877.
 99. Arshad, S.N., M. Naraghi, and I. Chasiotis, *Strong carbon nanofibers from electrospun polyacrylonitrile*. *Carbon*, 2011. **49**(5): p. 1710-1719.
 100. Liu, J., Z. Yue, and H. Fong, *Continuous Nanoscale Carbon Fibers with Superior Mechanical Strength*. *Small*, 2009. **5**(5): p. 536-542.
 101. Ruiz-Rosas, R., et al., *The production of submicron diameter carbon fibers by the electrospinning of lignin*. *Carbon*, 2010. **48**(3): p. 696-705.
 102. Huang, J., et al., *Electrospun Palladium Nanoparticle-Loaded Carbon Nanofibers and Their Electrocatalytic Activities towards Hydrogen Peroxide and NADH*. *Advanced Functional Materials*, 2008. **18**(3): p. 441-448.
 103. Chen, I.H., C.-C. Wang, and C.-Y. Chen, *Fabrication and characterization of magnetic cobalt ferrite/polyacrylonitrile and cobalt ferrite/carbon nanofibers by electrospinning*. *Carbon*, 2010. **48**(3): p. 604-611.
 104. Im, J.S., S.-J. Park, and Y.-S. Lee, *Preparation and characteristics of electrospun activated carbon materials having meso- and macropores*. *Journal of Colloid and Interface Science*, 2007. **314**(1): p. 32-37.
 105. Im, J.S., et al., *The effect of embedded vanadium catalyst on activated electrospun CFs for hydrogen storage*. *Microporous and Mesoporous Materials*, 2008. **115**(3): p. 514-521.
 106. Oh, G.-Y., et al., *Preparation of the novel manganese-embedded PAN-based activated carbon nanofibers by electrospinning and their toluene adsorption*. *Journal of Analytical and Applied Pyrolysis*, 2008. **81**(2): p. 211-217.
 107. Lee, J.S., et al., *Ketjenblack Carbon Supported Amorphous Manganese Oxides Nanowires as Highly Efficient Electrocatalyst for Oxygen Reduction Reaction in Alkaline Solutions*. *Nano Letters*, 2011. **11**(12): p. 5362-5366.
 108. Ahmad, Z., F. Al-Sagheer, and N.A. Al-Awadi, *Pyro-GC/MS and thermal degradation studies in polystyrene-poly(vinyl chloride) blends*. *Journal of Analytical and Applied Pyrolysis*, 2010. **87**(1): p. 99-107.
 109. Kercher, A.K. and D.C. Nagle, *Microstructural evolution during charcoal carbonization by X-ray diffraction analysis*. *Carbon*, 2003. **41**(1): p. 15-27.
 110. Mochida, I., C.H. Ku, and Y. Korai, *Anodic performance and insertion mechanism of hard carbons prepared from synthetic isotropic pitches*. *Carbon*, 2001. **39**(3): p. 399-410.
 111. Moon, S., J. Choi, and R.J. Farris, *Highly porous polyacrylonitrile/polystyrene nanofibers by electrospinning*. *Fibers and Polymers*, 2008. **9**(3): p. 276-280.
 112. Peng, M., et al., *Nanoporous structured submicrometer carbon fibers prepared via solution electrospinning of polymer blends*. *Langmuir*, 2006. **22**(22): p. 9368-9374.
 113. Maldonado, S. and K.J. Stevenson, *Influence of nitrogen doping on oxygen reduction electrocatalysis at carbon nanofiber electrodes*. *Journal of Physical Chemistry B*, 2005. **109**(10): p. 4707-4716.
 114. Lefevre, M., et al., *Iron-Based Catalysts with Improved Oxygen Reduction Activity in Polymer Electrolyte Fuel Cells*. *Science*, 2009. **324**(5923): p. 71-74.
 115. Rahaman, M.S.A., A.F. Ismail, and A. Mustafa, *A review of heat treatment on polyacrylonitrile fiber*. *Polymer Degradation and Stability*, 2007. **92**(8): p. 1421-1432.

116. Deng, D., et al., *Toward N-Doped Graphene via Solvothermal Synthesis*. Chemistry of Materials, 2011. **23**(5): p. 1188-1193.
117. Liu, R.L., et al., *Nitrogen-Doped Ordered Mesoporous Graphitic Arrays with High Electrocatalytic Activity for Oxygen Reduction*. Angewandte Chemie-International Edition, 2010. **49**(14): p. 2565-2569.
118. Chen, Z., D. Higgins, and Z.W. Chen, *Electrocatalytic activity of nitrogen doped carbon nanotubes with different morphologies for oxygen reduction reaction*. Electrochimica Acta, 2010. **55**(16): p. 4799-4804.
119. Chen, Z., et al., *Highly Active and Durable Core–Corona Structured Bifunctional Catalyst for Rechargeable Metal–Air Battery Application*. Nano Letters, 2012. **12**(4): p. 1946-1952.
120. Suntivich, J., et al., *Electrocatalytic Measurement Methodology of Oxide Catalysts Using a Thin-Film Rotating Disk Electrode*. Journal of the Electrochemical Society, 2010. **157**(8): p. B1263-B1268.
121. Wang, P., et al., *Origin of the catalytic activity of graphite nitride for the electrochemical reduction of oxygen: geometric factors vs. electronic factors*. Physical Chemistry Chemical Physics, 2009. **11**(15): p. 2730-2740.